Title

Mesoscopic oblique plane microscopy (Meso-OPM) - enabling large-scale 4D isotropic cellular resolution imaging with a diffractive light sheet

Wenjun Shao,[1,2] Minzi Chang[1], Kevin Emmerich[1], Patrick O Kanold[1], Jeff S Mumm[1], Ji Yi,[1,2,*]

Affiliations

[1]Department of Biomedical Engineering, Johns Hopkins University, Baltimore, Maryland, 21231, USA.
[2]Department of Ophthalmology, Johns Hopkins University, Baltimore, Maryland, 21231, USA.
* jiyi@jhu.edu

Abstract

Fundamental understanding of large-scale dynamic connectivity within a living organism requires volumetric imaging over a large field of view (FOV) at biologically relevant speed and resolution. However, most microscopy methods make trade-offs between FOV and resolution or imaging speed, making it challenging to observe highly dynamic processes at cellular resolution across mesoscopic scales (*e.g.*, whole zebrafish larva). To overcome this limitation, we have developed mesoscopic oblique plane microscopy (Meso-OPM) with a diffractive light sheet. By augmenting the illumination angle of the light sheet with a transmission grating, the axial resolution was improved ~7-fold over existing methods and ~2-fold beyond the diffraction limitation of the primary objective lens. We demonstrated an unprecedented FOV up to 5.4 × 3.3 mm with resolution of 2.5× 3 × 6 μm, allowing volumetric imaging of cellular structures in an uncleared brain slice with a single scan. Applying Meso-OPM for *in vivo* imaging of zebrafish larvae, we report here the first whole fish volumetric recordings of neuronal activity at 2 Hz volume rate and the first example of whole fish volumetric recordings of blood flow dynamics at 5 Hz with isotropic cellular resolution.

Introduction

Modern microscopy, in conjunction with genetically-encoded fluorescent reporters, (*1–4*) has greatly advanced fundamental studies in neuroscience, cardiovascular biology, and developmental biology. As many dynamic biological processes are interconnected across anatomical structures, rapid high-resolution volumetric imaging over a wide FOV is critical to interrogating complex molecular and cellular interactions in living organisms(*5–7*). For example, neuronal signals often traverse large distances within the brain to coordinate functions(*6, 7*). However, volumetric recording of neuronal activity patterns with sufficient FOV, resolution, and speed is a significant challenge due to the physical limit of optical diffraction. Microscopy techniques using a single primary objective are generally constrained by this limit, such as confocal, multiphoton, light field, and oblique plane microscopy, dictated by the numerical aperture (NA) of the objective used. This necessitates trade-offs between FOV and spatial resolution. For example, near-centimeter or multi-millimeter FOV can be obtained with sub-cellular lateral resolution by using low numerical aperture (NA) objective lens (e.g, NA = 0.35), but the axial resolution is typically above ~15 μm which is insufficient to resolve cellular features in the z-dimension (*8–13*). The diffraction limit also extends to microscopy methods that deliver illumination and collect fluorescence via the same refractive optics. For example, a computational miniature mesoscope used a micro-lens array instead of a regular objective lens to overcome the trade-

off between FOV and resolution. Yet, the axial resolution is limited by the total angular coverage of the micro-lens array leading to axial resolution of hundreds of microns(*14*).

The diffraction limit also poses an additional challenge in that axial resolution deteriorates more rapidly than lateral resolution with increasing FOV, since the depth of focus is inversely proportional to the square of NA. Thus, a much higher NA is needed to achieve axial cellular resolution than cellular lateral resolution. As a reference point, NA of ~0.6 and ~0.47 are needed for two-photon (900 nm excitation wavelength) and single-photon (488 nm excitation wavelength) excitation to achieve cellular axial resolution, respectively(*15*, *16*). Whereas the FOV of a high NA objective lens is fundamentally confounded by the scale-dependent geometric aberrations of its optical elements(*17*), the increase in NA is at the cost of FOV. Consequently, the FOV is usually less than 1 mm^2 (*18–23*) when utilizing high NA objective lens, which is insufficient for imaging dynamic events over large scales. While tremendous efforts have been made to design objectives to achieve large-scale recording with cellular resolution, particularly in the z-dimension, the physical limit of diffraction still persists(*9*, *12*, *15*, *16*), and the complexity of the optics and imaging system also increases dramatically.

Another strategy for overcoming the diffraction limit is to introduce additional optical elements so that resolution is not solely defined by the primary objective lens. The prominent example is to use two objectives to decouple excitation and detection as in light sheet microscopy (LSM)(*24*, *25*), selective plane illumination microscopy(*26*), dual-inverted selective-plane illumination microscopy(*27*), lattice light-sheet microscopy(*28*, *29*), light-sheet theta microscopy (*30*), and open-top light-sheet microscopes(*31*). While the primary objective offers lateral resolution, the excitation lens independently creates a thin optical light sheet therefore the axial resolution is no longer constrained by the primary objectives. These detection architectures usually have limited sample mounting space and require mechanical Z-stacking and stitching to image large samples, which is challenging for imaging fast dynamics in large-scale biological specimens.

So far, mesoscale volumetric imaging of live samples over multi-millimeter scales with isotropic cellular resolution and biologically relevant temporal resolution remains a tremendous challenge. In this paper, we introduce Meso-OPM which employs a novel strategy of using a diffractive light sheet to overcome the inherent limitations mentioned above. Meso-OPM belongs to a family generally termed single objective light sheet microscopy (SOLSM). In contrast to conventional LSM, which uses two objective lenses, SOLSM uses only a single objective lens but applies an off-axis oblique light sheet excitation at the specimen and a remote focusing system to capture the scanning light sheets at a fast frame rate. Because regular SOLSM uses one primary objective, the resolution limitations described above still apply. Meso-OPM overcomes this persistent problem by creating a high angle illumination light sheet with a transmission grating. This enables the axial resolution to be improved by 7-fold, i.e., to cellular level even when a low NA primary objective lens (e.g, NA = 0.3) is utilized. With isotropic cellular resolution enabled for off-the-shelf low NA objective lenses, we demonstrate an unprecedented FOV of 5.4 × 3.3 × 0.33 mm in an acute brain slice preparation at a resolution of 2.5× 3 × 6 µm, to resolve individual neurons. Using Meso-OPM to image living larval zebrafish, we also demonstrated whole-brain cellular resolution imaging of calcium dynamics at 2 Hz and whole-body blood flow imaging at 5 Hz.
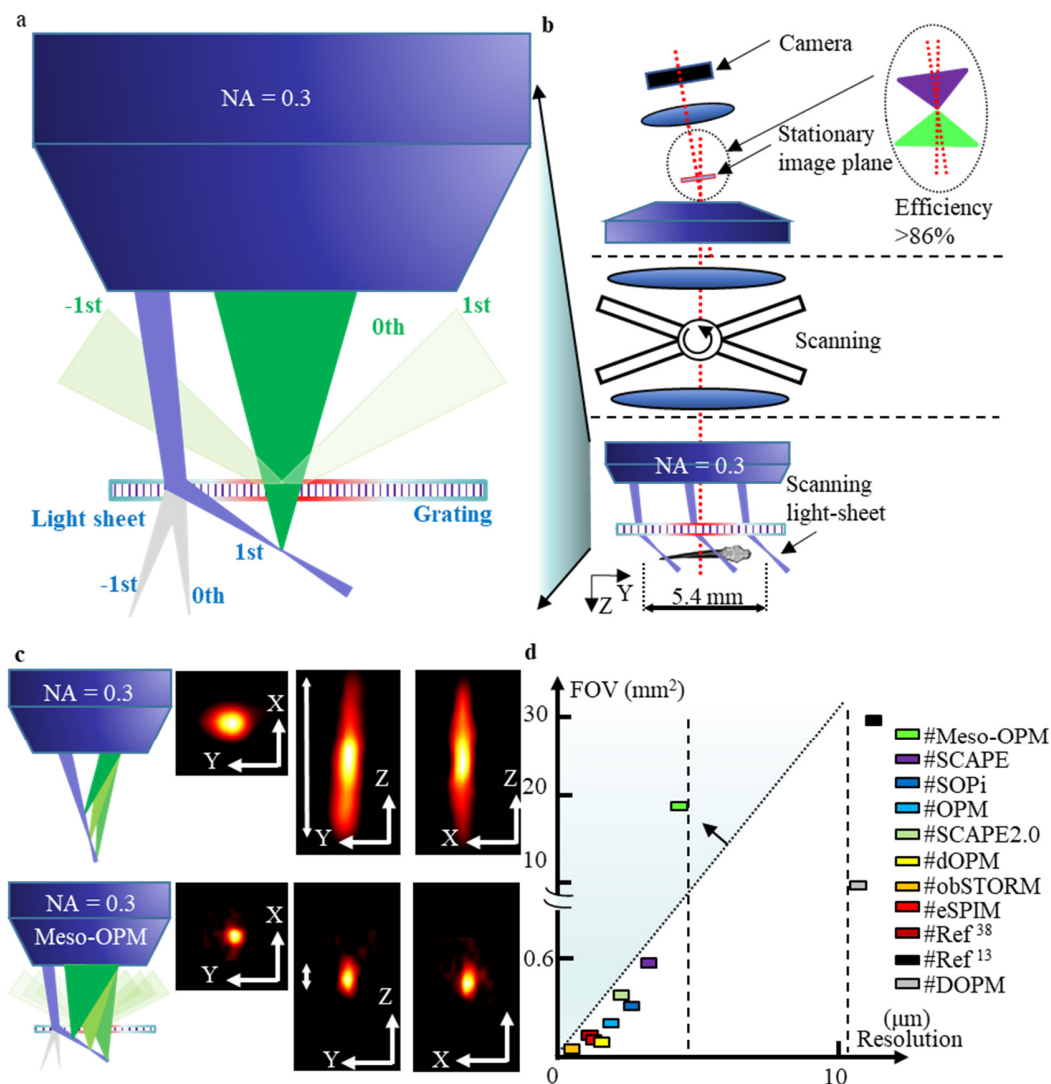
Fig. 1. The concept of volumetric imaging with a diffractive light sheet. (**a**) High-angle light sheet illumination in 1st order and full NA fluorescence collection in 0th order with the help of transmission grating. (**b**) The concept of utilizing diffractive light sheet in Meso-OPM to achieve large FOV and isotropic cellular resolution; (**c**) The comparison of spatial resolution with existing mesoscopic OPM. (**d**) The comparison of the FOV and resolution between different SOLSMs.

Results

The working principle of Meso-OPM

The limitation of previous mesoscopic OPM methods is the inherent trade-off between FOV and resolution, particularly depth and temporal resolutions. For low NA objective (e.g., NA=0.3), the axial resolution is in order of tens of microns. To circumvent the depth trade-off, we introduced a diffractive light sheet by using a transmission grating (Fig. 1a). Large angle diffractive light sheet can be created in 1st order while maintaining the full collection angle for emission collection in 0th order. The additional diffraction is independent of NA of the primary objective lens, and thus can improve the depth resolution significantly. The concept of the working principle for the proposed Meso-OPM is shown in Fig. 1b. To address temporal resolution limits, we leverage the remote focusing and the de-scanning scheme of SOLSM, with Meso-OPM reimaging the scanning high-angle light sheets onto a stationary intermediate image plane, thus achieving volumetric light-sheet imaging with fast frame rate over a large FOV with low NA optics. A large angle excitation needs only a slightly angled remote system, and thus increases the light collection efficiency from

35%(*10, 13*) to 86% (Fig. 1b). Altogether, the diffractive light sheet yielded a 7-fold improvement in axial resolution(*10, 13*) compared to standard mesoscopic OPM (Fig. 1c) and a 2-fold enhancement of the diffractive-limited axial resolution of an objective lens with 0.3 NA (Fig. S1 and S2), thus achieving isotropic cellular resolution. We compared FOV and resolution by Meso-OPM with an array of SOLSM techniques(*10, 13, 19, 32–38*) (Fig. 1d), and found that Meso-OPM eliminates the need to choose between FOV and cellular resolution for volumetric imaging. Consequently, Meso-OPM has the capability of capturing 4D biological dynamics at cellular resolution across FOV dimensions that have been challenging to achieve previously.

FOV and resolution characterization

As the angle of the diffractive light sheet is also a function of the excitation wavelength, we performed imaging experiments on two types of fluorescent microspheres to evaluate the FOV and resolution under blue and green light excitation. The FOV under different excitation wavelengths is the same, which is 3.3 mm (X) × 5.4 mm (Y) × 0.33 mm (Z) (Supplement Fig. S1 and S2). As the Y direction is the scanning direction, the FOV in the Y direction is not limited by the sensor size of the camera and thus is larger than that of the X (See *Supplement*). The resolution was quantified by calculating the full width at half maximum of the line intensity along X, Y, and Z directions of different bead volumes. The resolutions along X, Y, and Z direction for green light (561 nm laser) excitation are 2.9 μm, 3.5 μm, and 6 μm, respectively, while that for blue light (488 nm laser) excitation are 2.5, μm, 3 μm, and 6 μm, respectively (Supplement Fig. S1 and S2). By dividing the accessible FOV of 3.3 mm × 5.4 mm× 0.33 mm by the volumetric resolution of 2.5 μm ×3 μm× 6 μm, the information throughput of our Meso-OPM can be estimated to be ~1.3 × 10^8 resolvable image points across the imaged volume. By extension, this suggests the ability to monitor 4D signal dynamics of ~1.3 × 10^7 cells.

High-resolution structure imaging in whole larval zebrafish and uncleared acute mouse brain slice

Whole larval zebrafish imaging with Partial FOV

After characterizing the FOV and resolution, we carried out structure imaging of large living samples to test system performance. We first imaged transgenic zebrafish larvae that express a green fluorescent protein reporter in vasculature endothelial cells at 4 days post fertilization (dpf). The approximate dimensions of a zebrafish larvae at this age are ~3-4 mm (X) × ~0.6 mm (Y) × ~0.5 mm (Z)(*39*). The acquired volume data has dimensions of 3.3 mm (X) × 0.65 mm (Y) × 0.55 mm (Z) with pixel density of 2048 × 300 × 275 pixels (acquiring XZ plane at a frame rate of ~500 Hz). By achieving isotropic cellular resolution over a wider and deeper FOV, we can provide a high-definition 3D rendering of the whole larva at a frame rate of 500 Hz (See supplement video 1).

Color-coded projections of volumetric data demonstrate the ability of Meso-OPM to resolve individual blood vessels throughout larval zebrafish larva in 3D (Fig. 2a-c). The branches of the mesencephalic vein (MsV) in the dorsal head region and the intersegmental veins (ISV) in the ventral trunk can be observed in both the lateral and axial projections (Fig. 2a-c). Thanks to the large FOV, the whole dorsal longitudinal anastomotic vessel (DLAV), which has a length of ~ 3 mm, can be fully visualized in the lateral (Fig. 2a) and axial views (Fig. 2c). The DLAV is connected to either dorsal aorta (DA) or posterior (caudal) cardinal vein (PCV) by ~29 pairs of ISVs over a distance of ~3 mm (Fig. 2c). The ability to discriminate all ISVs demonstrates that a depth penetration of ~250 μm can be maintained throughout the FOV (Fig. 2c). The intensity profile of the small feature along the depth direction suggests depth resolution better than 6.5 μm (white dash box shown in

Fig. 2c), which is sufficient to resolve individual vessels in the depth direction. The double-edge structure of the ISV vessels can be revealed by the intensity profile of a single ISV (blue dash box shown in Fig. 2c). Transverse views of the trunk at four rostral-caudal positions clearly reveal the round shape of the neural tube (NT) and notochord (NC) (Fig. 2d) which typically have a diameter of ~25 μm and 50 μm, respectively(*40*). *Enface z*-projections of the head region at six different depths demonstrate the ability to resolve individual vessels throughout the imaging volume (Fig. 2e-j). The discrimination of different vessel patterns, such as the paired brain vascular structures, indicates the depth resolution and penetration can be well maintained in the peripheral area of the FOV.
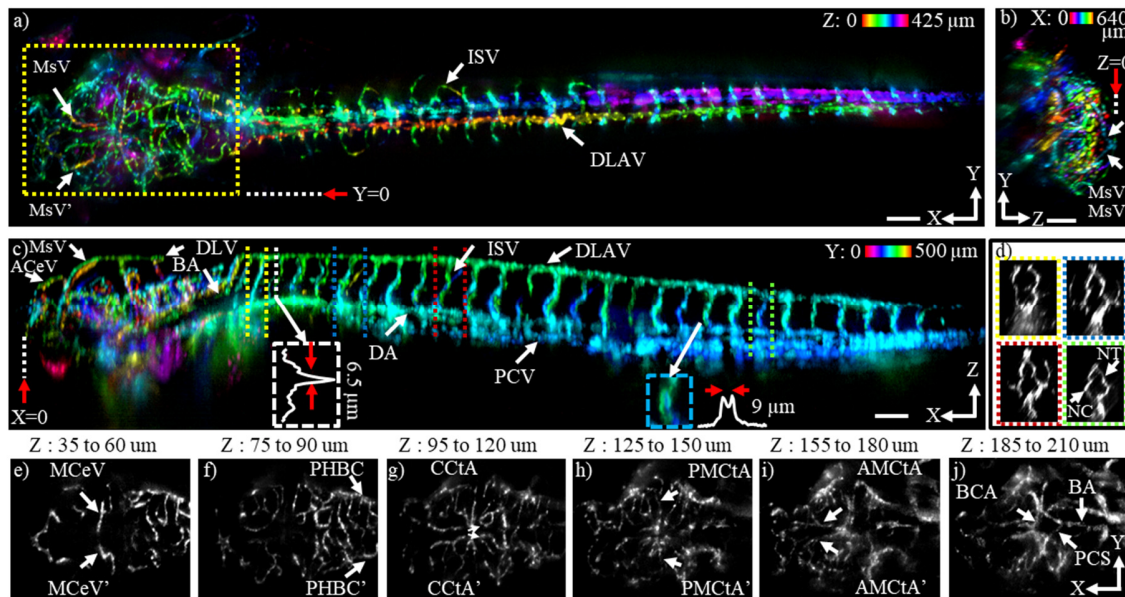

Fig. 2. High-definition whole-body vasculature imaging of live zebrafish larva obtained in a single FOV at frame rate of 500 Hz. (**a**) Color-coded maximum intensity projection (MIP) in the XY plane over 425 μm along the Z direction. The 0 reference position of the MIP is marked by a red arrow in panel b; (**b**) Color-coded MIP in the YZ plane over 640 μm along the X direction indicated by the yellow dashed box in panel a. The 0 reference position of the MIP is marked by a red in panel c; (**c**) Color-coded MIP in XZ plane over 500 μm along the Y direction. The 0 reference position of the MIP is marked by a red arrow in panel a. (**d**) YZ cross-sections of 4 pairs of ISVs indicted by corresponding double dash lines in panel c; (**e-j**) *Enface z*-projections of the head region marked by yellow dashed box in panel a. Paired vessel structures such as MCeV (Middle cerebral vein), PHBC (Primordial hindbrain channel), CCtA (Cerebellar central artery), PMCtA (Posterior mesencephalic central artery), AMCtA (Anterior mesencephalic central artery), and PCS (Posterior communicating segment) can be seen within different projections. Scale bar, 100 μm. (BCA: Basal communicating artery; BA: Basilar artery.)

Uncleared acute mouse brain slice imaging with Full FOV

We next imaged an acute mouse brain slice with calretinin-neurons expressing tdTomato under the full FOV of 3.3 mm (X) × 5.4 mm (Y) × 0.33 mm (Z) with a pixel density of 2048 × 2000 × 160 pixels at frame (XZ plane) rate of 100 Hz. To eliminate the background by the 0th and -1st order diffraction by the grating, a synchronized moving aluminum foil is used as a beam blocker allowing only 1st order diffraction excitation during the acquisition (See Fig. S3d in supplementary material). The 0th and -1st order diffraction can be effectively removed by customizing the transmission grating. Figure 3a shows a single scan color-coded mesoscopic FOV covering major anatomical structures such as cortex, hippocampus, thalamus. The uniform somatic structures indicate the cellular resolution is well maintained over the full FOV. Neuronal somas are clearly visualized from cortical layer I to IV in all three projections (Fig. 3a-3d), confirming 3D isotropic cellular resolution. The large FOV allows us to simultaneously capture neurons in the hippocampus (Fig. 3e and 3f) and the

thalamus (Fig. 3g and 3h). Close examination demonstrates the capability to image apical dendrites of pyramidal neurons in layer VI (Fig. 3i). A high-definition 3D rendering of the acquired volume can be found in supplementary video 2.
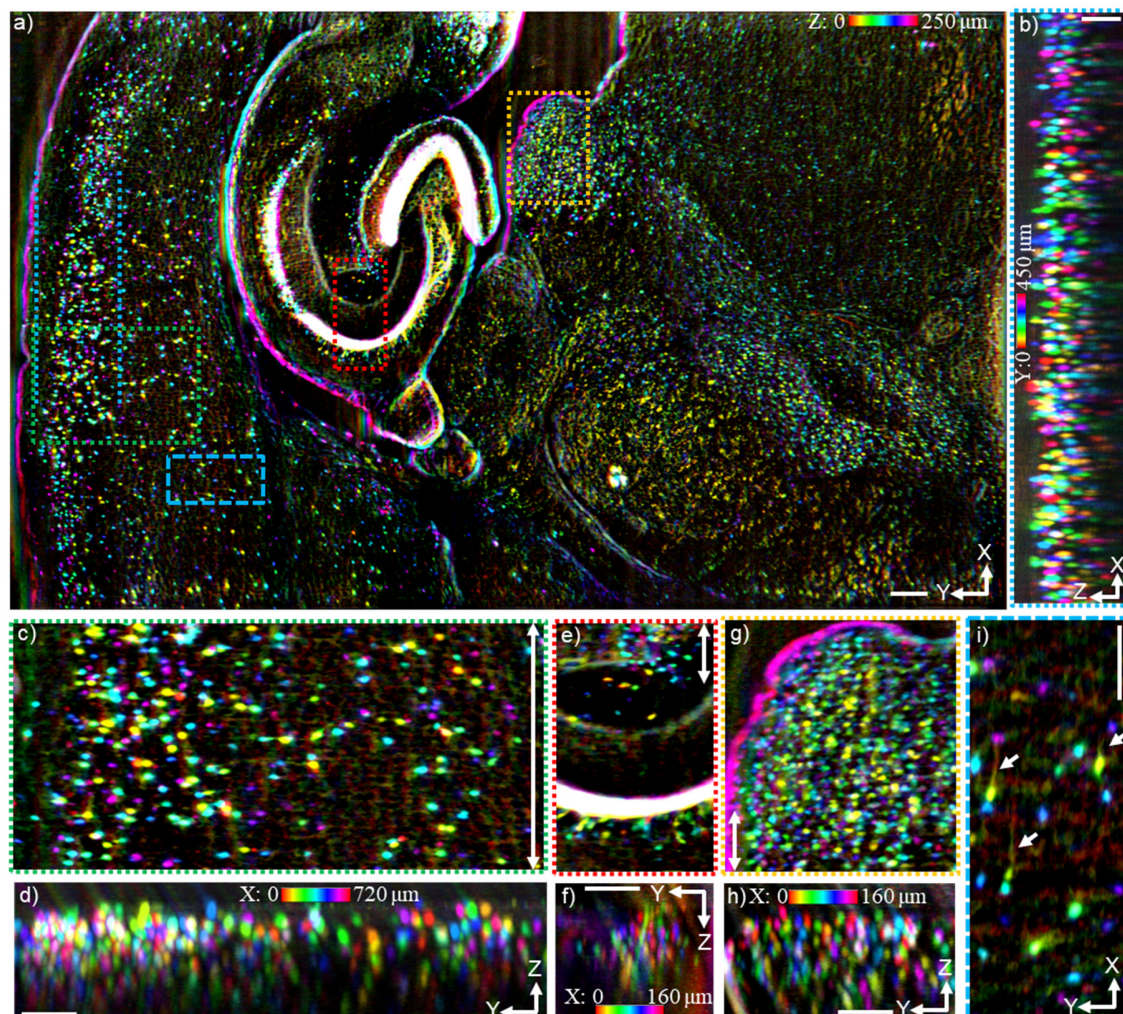

Fig. 3. High-definition 3D imaging of an acute brain slice obtained in a single FOV at isotropic cellular resolution across a wide FOV. (a) Color-coded MIPs of the *enface* view over a distance of 250 µm in the Z dimension, i.e., the whole brain slice volume. **(b)** Color-coded MIPs of the XZ plane over a distance of 450 µm in the Y dimension. The 0 reference positions of the projections are indicated by blue dash lines in panel a; **(c, e, and g)** Zoomed images of the *enface* views of the areas indicated by dashed boxes in panel a; **(d, f, and h)** Color-coded MIPs of the YZ plane of the volume indicated by double arrow lines in panel (c, e and g). The scale bar for panel (b) is 200 µm; the scale bars for the other panels are all 100 µm.

Whole-body recording of neuronal activity in zebrafish larvae

After characterizing FOV and resolution in static images of living samples, we proceeded to image neuronal signaling dynamics across an entire zebrafish larva expressing a cytosolic genetically encoded calcium indicator (jGCaMP7s) in neurons throughout the central nervous system. The whole 4day old zebrafish body covered an area of ∼ 3.3 mm × 0.5 mm × 0.4 mm. Color-coded maximum intensity projections (MIPs) of the whole zebrafish larvae are shown in Fig. 4a-c. The entire volume data has a pixel dimension of 2048 × 125 × 200 pixels (each volume contains 125 planes) which was acquired at a volume rate of 2 Hz. Thanks to the large FOV, individual neuronal features can be identified throughout the entire nerve system from the brain to the spinal cord, as shown in the *enface* projection (Fig.

4a), as well as the side projection (Fig. 4b). MIPs of different brain regions at varying depths were generated (Fig. 4c-f). Distinct features can be clearly delineated, such as the boundary of the hemispheres indicated by the yellow arrows in Fig. 4c-f and the boundary of the optic tectum in Fig. 4g. For instance, tectal neurons in the midbrain can be clearly discerned (Fig. 4c,g and 4d,h), as well as neurons in the cerebellum (Fig. 4e,i). Pallium and habenula neurons that couldn't be seen in Fig. 4c-e) can be seen in a deeper layer MIP (Fig. 4f,j), which agrees with the anatomy structure of the zebrafish brain(*41*, *42*). Zoomed images of the boxed areas in Fig. 4g-j further confirm that individual neurons can be well resolved at different tissue depths. A comparison of the image acquired with the Meso-OPM and the confocal microscope is provided in supplement material (Fig. S4) showing the similar anatomical organization of neurons.

Calcium dynamics over the entire zebrafish nervous system were captured at a volume rate of 2 Hz for 1.5 min. To evaluate spontaneous calcium signals in individual cells, 60 neurons were manually selected at different depths throughout the brain and spinal cord (Fig. 4l) and fluorescence intensity traces plotted over an 85s recording period (Fig. 4n). These data show that at two time points many of the selected neurons appeared to fire synchronously. This correlated firing pattern can also be observed in supplementary video 3. As the FOV covers the whole larva, Meso-OPM offers a unique opportunity to study how neuronal activities are correlated over large volumes encompassing the entire brain and spinal cord, a level of inquiry that has been inaccessible to date. A 4D rendering of the time series can also be found in supplementary video 3.
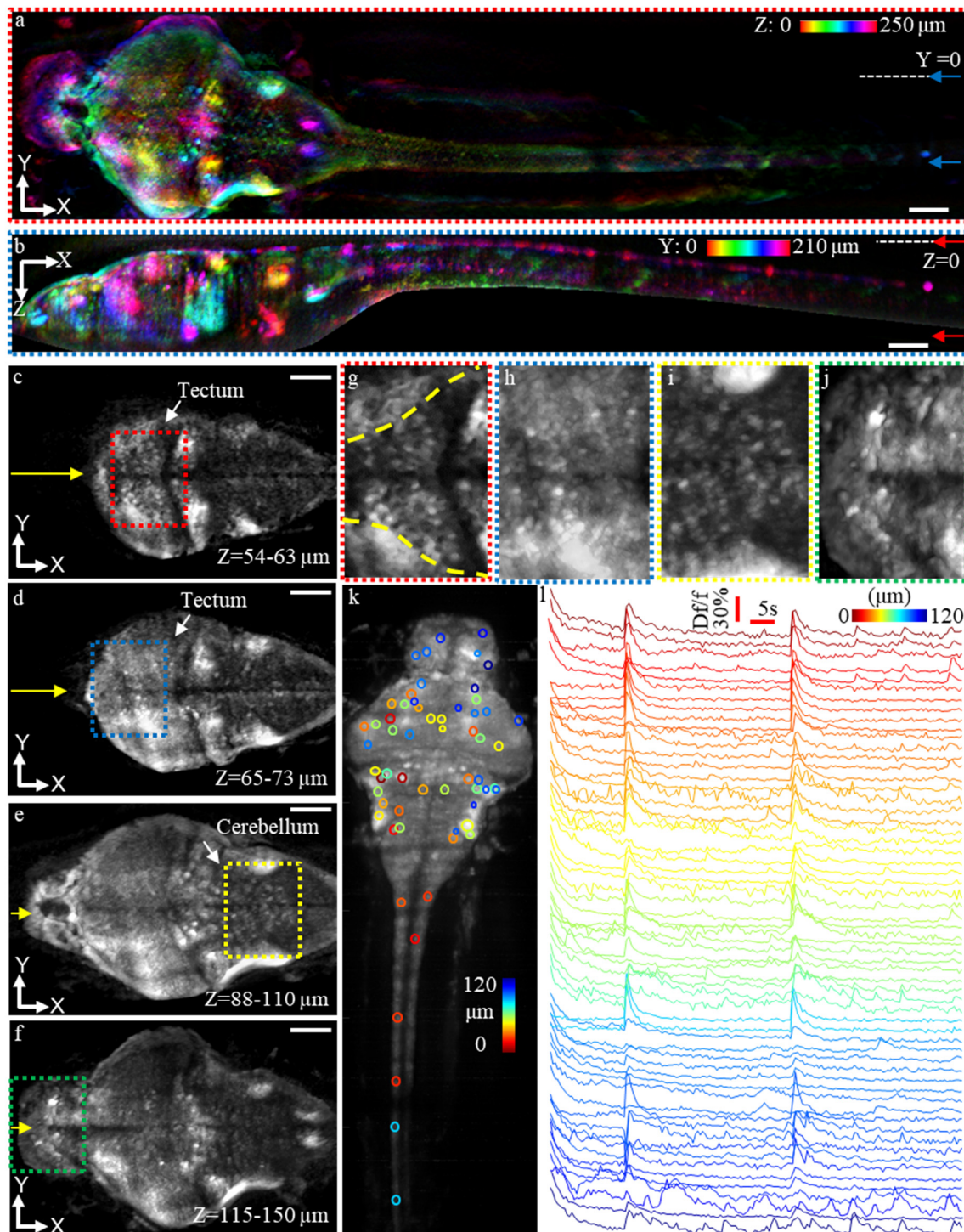
Fig. 4. Whole-body neuronal activity recording in zebrafish larva with isotropic cellular resolution. (**a**) Color-coded MIP in XY plane over 250 μm along the Z dimension. The reference positions of the MIP are marked by arrows in panel b. (**b**) Color-coded MIP in XZ plane over 210 μm in the Y dimension. The reference positions of the MIP are marked by arrows in panel a. (**c-f**) *Enface* projections at different z-depths across the whole brain. (**g-j**) Zoomed views of the boxed areas in panels c-f. (**k**) Representative neurons selected for evaluating correlated activity patterns are marked with circles, the color represents relative imaging depth from 0 to 120 μm. Fish data shown in a-k were acquired at 250 Hz per plane and scanning 125 planes at ~4 μm spacing, thus a 2 Hz whole-volume resolution. (**l**) Calcium traces of the selected neurons (see panel l) over an 85 s recording period. Scale bar, 100 μm.

Imaging blood flow over the whole larval zebrafish at high spatiotemporal resolution

By achieving large-field isotropic cellular resolution across entire sample volumes without moving the sample or objective lens, our novel Meso-OPM method is well-suited for imaging cellular dynamics across whole organisms or whole tissues at fast speeds. As an additional demonstration of this, we performed volumetric imaging of blood flow using a transgenic zebrafish expressing enhanced green fluorescent protein (EGFP) in myeloid cells. The structure of the entire larval fish was firstly confirmed by the single volume shown in Fig. 5a. Next, images were acquired across a whole 4-day old zebrafish larva (an ~3.3 mm × 0.5 mm × 0.5 mm volume) with pixel dimensions of 2048 × 125 × 250 pixels at a volume rate of 5 Hz, which was able to capture cardiac cycles (See supplement video 4), and each volume containing 125 planes. Results of timelapse imaging over a 9s time window show individual cell dynamics within major vessels of the circulatory system, such as the CA, caudal vein (CV), dorsal longitudinal anastomotic vessel (DLAV), intersegmental veins (ISV), posterior (caudal) cardinal vein (PCV), and dorsal aorta (DA) (Fig. 5b and c). Cell movements are indicated by color-coded temporal traces (Fig. 5b and c). Owing to the fast volume rate, there are no motion artifacts caused by the movement of the blood cells. The discrimination of individual blood cell movements in 3D across the whole FOV, from heart to tail, further demonstrates the high temporal and spatial resolution possible with Meso-OPM (See 4D rendering in supplementary video 4). To quantify blood flow, motion contrast angiography (See *Material and methods*) was performed on the whole time series. An *enface* projection of the angiogram in which the static features are removed highlights the movement of the blood cells (Fig. 5d, compared to Fig. 5b).

To exemplify the power of the high spatiotemporal resolution achieved, the 4D trajectory of a single cell traveling within an ISV from the DLAV to the CV over a time window of 4 s is provided in Fig. 5e-g. As a result of fast volume rate, the captured movements match the shape of the ISV. With the capability of tracking individual cells in 4D over a large FOV, we are able to quantify the speed of blood flow in different types of vessels such as the DA, PCV, ISV (Fig. 5h). The measured results agree with previous publications(*43*) revealing different velocities in each vessel type. For example, the velocity of the blood cell in the DA is faster than in the PCV or ISV, which is as expected. Similarly, the pulsatile movement of the blood cells in the DA and PCV is more apparent than in ISV. Owing to the large FOV, blood cells in the DA were tracked over a distance of ~2 mm from the heart to the tail. An interesting observation is that the velocity in the DA gradually slows down as the blood cell are traveling away from the heart.
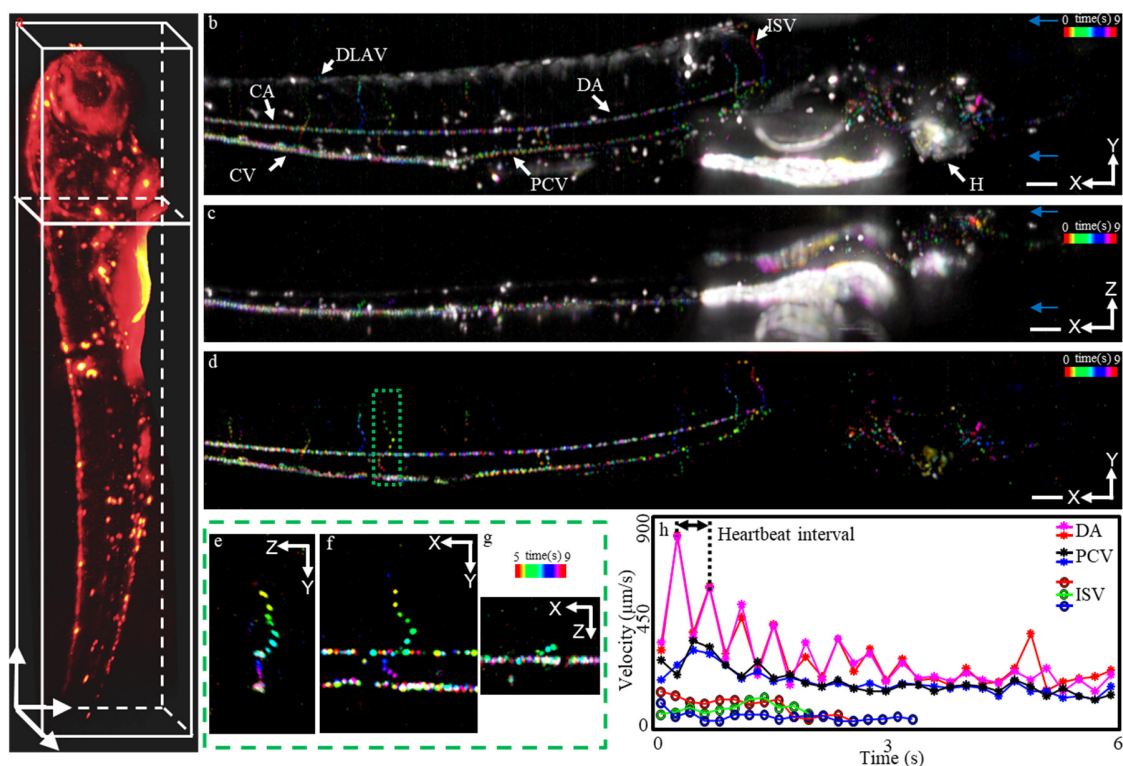
Fig. 5. Imaging blood flow over the whole larval zebrafish at high spatiotemporal resolution. (**a**) Single volume captured at volume rate of 1 Hz to highlight the structure. (**b**) Color-coded MIP of cell movements in the XY plane. The XY view is generated by spatial MIP along Z direction over the position indicated by blue arrows in panel c; (**c**) Color-coded MIP of cell movements in the XZ plane. The XZ view is generated by spatial MIP along Y direction over the position indicated by blue arrows in panel b; (**d**) Color-coded angiogram in XY plane. (**e-g**) The tracking of blood cells in 3D over a time window of 4 s in a single ISV indicated in panel e. Fish data shown in b-g were acquired at 625 Hz per plane and scanning 125 planes at ~4 μm spacing, thus a 5 Hz whole-volume resolution. (**h**) Measurement of velocities of blood cells in different types of vessels. The heart rate was estimated to be ~140 Hz by Fourier analysis. Scale bar, 100 μm.

Discussion

Our diffractive mesoscopic OPM leverages the large FOV of off-the-shelf low magnification objective lens (e.g., 0.3 NA) while overcoming the limitation of insufficient axial resolution. The use of diffractive light sheet in Meso-OPM allows 3D isotropic cellular resolution over a 3.3×5.4 mm^2 FOV without any mechanical translation. We demonstrated the performance by structural imaging of entire zebrafish larvae and a large acute brain slice. With large FOV and isotropic cellular resolution, and biologically relevant speed, we were able to record calcium dynamics over the entire zebrafish nerve system at volume rate of 2 Hz, which was previously unattainable due to insufficient depth resolution(*10, 13*) or limited FOV covering only the brain(*18, 25*). We also demonstrated single blood cell 4D tracking at volume rate of 5 Hz over the whole larval zebrafish. Imaging and quantifying dynamic cellular and signaling events between multiple tissues/regions, such as the recording of spontaneous neuronal activity between the brain and spinal cord, and blood cell circulation between multiple vessel types (e.g., from the DA to CA), has been an unmet challenge which Meso-OPM can overcome.

The optical performance of the current system can be further improved in several aspects. First, the current off-the-shelf transmission grating has significant -1st and 0th diffractions that we need to block when imaging large specimens such as the mouse brain. The transmission grating can be optimized to have polarization selectivity such that >90%

efficiency can be achieved in 1st order diffraction while other orders are negligible. While the spontaneous emission will experience loss passing through the grating, the overall collection efficiency is compensated by the higher collection efficiency at the remote focusing system. Second, we note that the grating can introduce spherical aberrations. However, the impact on our resolution is moderate due to the low NA objectives (See Fig. S5 in supplement). The aberration can also be mitigated or corrected by using thinner grating, better relay optics, and adaptive optics. Lastly, although we have demonstrated penetration of ~250 μm in acute brain slice over the full FOV, the image contrast can be further increased by utilizing confocal detection of a scanning light sheet(44).

In summary, we circumvent the theoretical limitation of insufficient axial resolution in low NA objective lens by creating a high angle diffractive light sheet. By avoiding the trade-offs between FOV, axial resolution, and imaging speed, we demonstrate 4D isotropic cellular resolution over a FOV that is unattainable previously.

Materials and Methods

System description

The layout of the optical design for Meso-OPM is shown in Fig. 6a). The key component that enables isotropic cellular resolution over large FOV in Meso-OPM is the transmission grating (TG) shown in Fig. 6b). The excitation light sheet (blue) in Fig. 6b) can be diffracted into different orders by the flowing equation

$$\theta_m = ar\sin((m\lambda + \sin(\theta_i)/a)),\tag{1}$$

where θ_m is the diffraction angle for m^{th} order, m represents the diffracted order, λ is the wavelength of the incident beam, θ_i is the incident angle, a is the line density of the TG. On the one hand, only the high-angle light sheet (blue) in 1st order can illuminate the sample, as shown in Fig. 6b (Also see supplementary Fig. S3b). On the other hand, only the emission fluorescence (green, pale green, yellow) in the 0th order is collected as the emission fluorescence in non-zero order are either rejected by the aperture of the objective lens (OL1) or widely separated in the image space (Fig. 6c and Supplementary Fig. S6). An examination of Eq. 1 finds that the angle of the diffraction angle can be increased by a high line density of the TG. With a large illumination angle, the axial resolution is improved beyond the limitation set by the NA of the objective lens (See supplementary Fig. S7d and 7e). Having described the mechanism of creating and imaging with the high-angle diffractive light sheet, we set out for detailed explanations of the whole system which can be divided into 3 subsystems: (1) the excitation light source unit; (2) the 3D reimaging unit; (3) the remote refocusing system.

The light source unit consists of laser (LS1: Coherent, 488nm, 50 mW; LS2: Coherent, 561nm, 100 mW), a Powell lens (PL: Edmund optics, 30° fan angle), two achromatic lenses (L5: Thorlabs, two AC254-050-A; L6: two AC254-250-A), two plane mirrors (M2 & M4: Thorlabs, PF10-03-P01), and one flip mirror (FM3: Thorlabs, FP90 and PF10-03-P01). Excitation light can be switched between LS1 and LS2 by FM3. PL has a fun angle of 30° and is used to convert the collimated laser beam into a uniform light sheet. PL is placed at the focal plane of L5. The length of the light sheet is ~10 mm which is controlled by the focal length of the L5. L5 and L6 work together as a beam expander to expand the width of the light sheet from 0.7 mm to 3.5 mm.

After the formation of the light sheet, a dichroic mirror (DM, Chroma, ZT488/561rpc-UF1) is used to guide the light sheet into the 3D reimage unit which consists of one transmission grating (TG: Thorlabs, GT13-12), two objective lenses (OL1: Olympus, UplanFL10×/0.3; OL2: Olympus, UPLSAPO 20×/0.75), two groups of relay lenses (L4, L3,

L2: Thorlabs, two AC508-200-A; L1: Thorlabs, two AC508-100-A), one plane mirror (Thorlabs, PF10-03-P01), one galvanometer (Nutfield: QS-12 OPD, 20 mm aperture). The optical path length between L6 and L4 is equal to the sum of their focal lengths. By moving the light source unit with the translation stage TS1, the light sheet is projected onto an off-center position of the DM to create an offset of 7 mm with respect to the optical axis of relay lens L4. After the 1:1 relay of L4 and L3, the light sheet is projected onto the galvanometer GM. GM is placed at the focal plane of both L3 and L2. With the scanning of the GM, an intersection line of the scanning light sheets was generated at the pupil plane of objective lens OL1 after the relay lens group of L2 and L1. Because the relay lens group of L2 and L1 has a magnification of 1:2, the length and the width of the light sheet were reduced to 5 mm and 1.75 mm, respectively. The offset of the intersection line with respect to the optical axis is also reduced by half, which is 3.5 mm. As a result of the offset, the light sheet has an incident angle of ~11º when projected on the transmission grating (TG: Thorlabs, line density of 0.83 μm/line) where it's divided into different diffraction orders (Fig. 6b). The angle of the diffractive light sheet can be calculated by Eq.1 before it's focused on the sample. As for 488 nm and 561 nm two light sources (LS1, LS2), the diffraction angle at 1st order can be calculated to be 51º and 60º, respectively. The reason for choosing grating with a line density of 0.83 μm/line is that too small angle of the light sheet will lead to poor axial resolution(10, 13) while too large angle will limit the detectable depth range (See supplementary Fig. S7f). The laser power at diffraction orders beyond -1st, 0th, and 1st are measured to be negligible. So we only consider diffraction in the -1st, 0th, and 1st. The distance between the 0th and the 1st is > 1mm at the sample. Consequently, the 0th excitation will not illuminate the sample is less than 1 mm in any dimension. As for the full FOV imaging, the 0th and -1st orders of the diffraction can be blocked by a moving aluminum foil(AF) (See supplementary Fig. S3b and 1c; Vedio 5) to avoid undesired fluorescence excitation. One of the glass windows (CG, diameter: 15 mm, thickness: 0.1 mm, refractive index: ~1.52) is used to protect the grating surface while the other one is served as a protective window. Given the focal length of OL1 (f = 18mm) and the width (3.5 mm) of the collimated light sheet on the pupil of OL1, the beam waist and Rayleigh range of the focused light sheet can be calculated. As for 488 nm from LS1, the beam waist and Rayleigh range are approximately 5 μm and 210 μm, respectively. As for 561nm from LS2, the beam waist and Rayleigh range are slightly bigger, which are 5.5 μm and 240 μm, respectively.

Next, the emission fluorescence is diffracted into three orders as they travel through the TG. Fortunately, diffracted light in the non-zero orders is either rejected by the aperture of OL1 or focused onto separated positions allowing only the acquisition of the 0th (See detail analysis in supplementary Fig. S6). Then, the 0th order emission is directed by the relay lens L1 and L2 and mapped back to GM where it is de-scanned. Owing to the de-scanning scheme, a stationary intermediate image plane (IIP) can be formed after OL2. To further increase the angle of IIP, the magnification from OL1 to OL2 is designed to be 1:4 by choosing the proper focal lengths of the relay lens group and OL2. The angle of IIP can be calculated to be 79º and 82º for excitation wavelengths of 488 nm and 561 nm, respectively(13). Finally, a high-angle stationary optical replica of the scanning light sheets is created by the 3D reimaging unit.

Finally, the remote focusing system consisting of the camera (Andor, Zyla 4.2), camera lens (Navitar: MVL75M1, f = 75 mm), optical filter (F1: Chroma, MF525-39; Thorlabs, AT575lp), objective lens (Olympus, UPLFLN40×/0.75;), and translation stage (2 axes of rotation and 3 axes of translation) is used to image the stationary IIP. The optical filter needs to be switched according to different excitation wavelengths. According to the angle of the IIP, the angle of the optical axis of OL2 and OL3 is 11º for 488nm excitation and 8º for 561

nm excitation. As can be seen from the zoom-in of the IIP in Fig. 6a), the IIP is almost perpendicular to the optical axis. The light collection angle of OL2 and OL3 is ~97º which can be calculated according to their NA. Given the titled angle between OL2 and OL3, the effective acceptance angle of the OL3 is 86 º and 89 º for 488nm excitation and 561nm excitation, respectively. Therefore, >86% (86/97) of the light from OL2 (green) propagates within the light collection cone of OL3 (purple). The control signal for the camera, the galvanometer mirror, and the motorized aluminum is shown in supplementary Fig. S8.
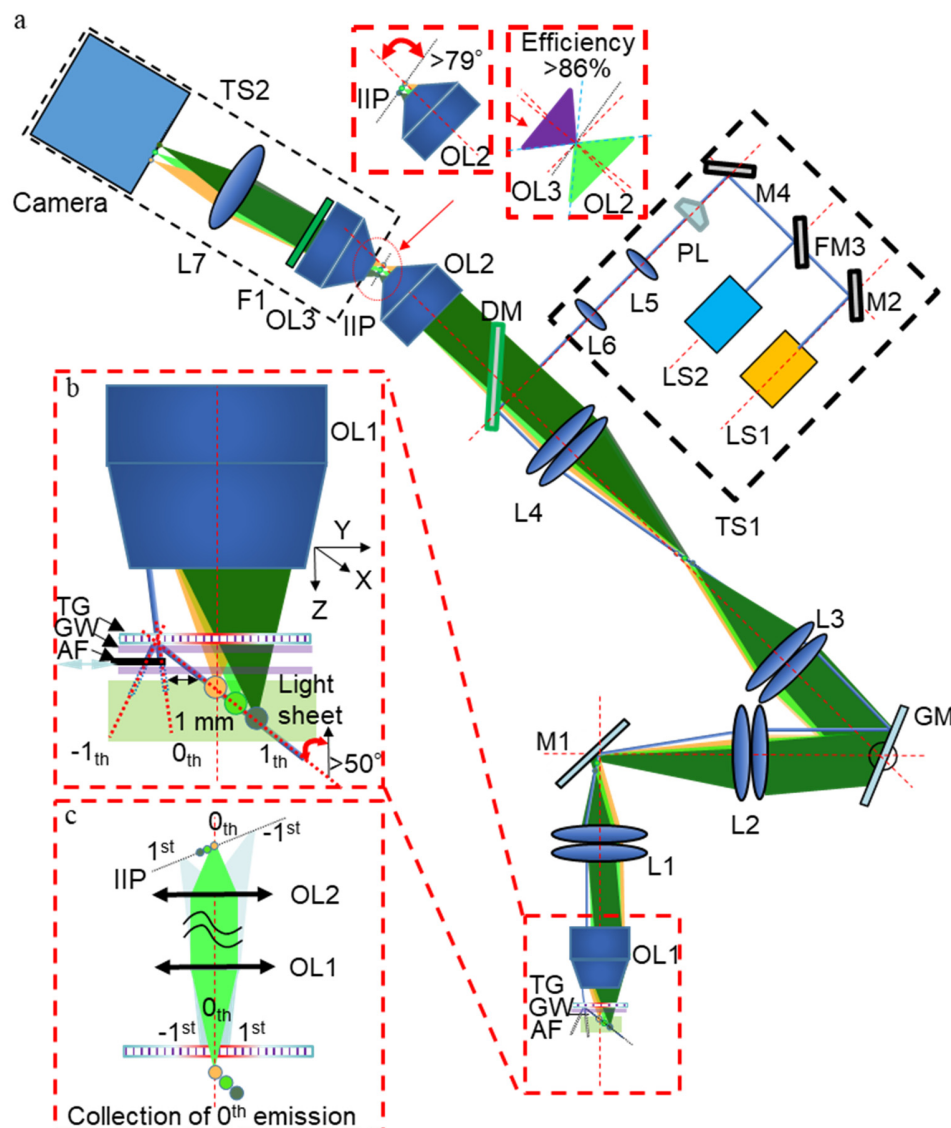

Fig. 6. The schematic of the experiment setup. (**a**) The layout of the whole optical design. TG: transmission grating; GW: glass window; AF: aluminum foil; OL: objective lens; L: lens; M: mirror; GM: galvanometer mirror; IIP: intermediate image plane; F: filter; TS: translation stage; PL: Powell lens; FM: flip mirror; LS: light source. (**b**) The zoom in view of the primary objective lens exhibiting the generation of high-angle excitation light sheet. The primary objective lens consists of the objective lens (OL1), transmission grating (TG), glass window (GW), the motorized aluminum foil (AF). (**c**) A simplified layout of the optics from the light sheet to the IIP showing the imaging of emission fluorescence in different diffraction orders.

The theoretical resolution

After the description of the setup, we now give the theoretical expression of the system resolution. As the angle of the excitation light sheet is disconnected from the NA of the primary objective lens (OL1), the calculation of the system point spread function (PSF) can be written as follows:

$$PSF_{Sys} = PSF_{Ill} \times PSF_{Det}, \tag{2}$$

where PSF_{Ill} is the illumination PSF, PSF_{Det} is the detection PSF. The calculation is the same with that for the LSM except for the non-orthogonality between the illumination and detection PSF. A numerical simulation based on our previous publications(44, 45) is used to calculate the theoretical resolution according to Eq.2 (See supplementary Fig. S7a). The axial resolution, as well as the axial detectable range under different illumination angles resulting from different line densities of the TG, are analyzed (See supplementary Fig. S7f). With the increase of the illumination angle, the axial resolution improves dramatically while the dateable axial range decreases. To obtain a detectable axial range of ~350 μm and axial resolution of ~5 μm, the line density is chosen to be 1200 lines/mm (0.83 μm/line). The calculated theoretical resolution of ~1 μm ×1.5 μm × 5 μm (488 nm laser) is slightly better than that of the measured resolution of ~2.2 μm × 3 μm × 6 μm (488 nm laser). This is probably due to the spherical aberration caused by the thickness of the TG and the aberrations from off-the-shelf lenses.

Data processing

As a result of the oblique illumination light sheet, the acquired image volume is a stack of oblique 2D images. Therefore, affine transformation consisting of both shearing and scaling is applied to the volume data to reconstruct the actual geometry of the sample (10, 33, 45).

As for fig. 4b and supplement video 3, the lower part of the fish data (mainly the digestive system) is removed to highlight the neuronal features in the brain and the spinal cord. To generate the 2D angiogram shown in Fig. 5d-g, every two adjacent volume data sets in the whole time series are subtracted to firstly generate a differential time series. Then, a 3D angiogram of the entire fish can be created by applying MIP along the time axis of the differential time series. Lastly, the enface projection (Fig. 5d-g) was obtained by taking MIP along the depth direction of the 3D angiogram.

Biological sample preparation

All animal-related procedures were in accordance with the Institutional Animal Care and Use Committee at Johns Hopkins University and conformed to the guidelines on the Use of Animals from the National Institutes of Health (NIH).

Red and green fluorescent microspheres (Polysciences: YG Microspheres, 1.00μm; Red Dyed Microsphere, 1.00μm) were used in the experiments for resolution characterization. They were diluted and immobilized in 1% agarose and molded in two separate Petri dishes. The Petri dish was covered with a cover glass (thickness: 0.1 mm, refractive index: ~1.52) to flat the gel surface. Water immersion is applied between the protective glass window of the objective lens and the cover glass before imaging.

Transgenic zebrafish larvae expressing green reef coral fluorescent protein in endothelial cells (Tg(VEGFR2:GRCFP)ZNL, Fig. 2), green fluorescent protein in macrophage cells (Tg(spi1b:GAL4,UAS:EGFP), Fig. 5), and genetically encoded calcium indicators (Tg(elavl3:jGCaMP7s), Fig. 4) were used in the *in vivo* experiments. Zebrafish at 4-5 dpf with length of 3-4 mm were cultivated at ~ 28°C following standard procedures (light cycle conditions of 14h light and 10 h dark). To mount samples, zebrafish larvae were first anesthetized with tricaine (MS-222) for ~3 minutes and then added to heated 1.5% low-

melting agarose in a Petri dish to allow for orientation at room temperature before providing overlayed E3 media following agarose hardening. The refractive index of the water is 1.33. The objective was immersed into the Petri dish to image the fish directly in an upright way. After the imaging, all of the zebrafish were released into freshwater for recovery.

For the in vitro slice imaging, progeny from homozygous Calb2-IRES-cre mice (JAX no. #010774) crossed with homozygous tdtomato reporter mice (JAX no. #007909) was used. To prepare the acute brain slice, the whole brain of a 4-weeks-old mouse was dissected out in artificial cerebrospinal fluid ACSF containing (in mM): 130 NaCl, 3 KCl, 1.25 NaH2PO4, 20 NaHCO3, 10 glucose, 1.3 MgSO4.7H2O, and 2.5 CaCl2.2H2O (pH 7.35–7.4, equilibrated with 95% O2–5% CO2). A 400-µm tissue block containing both thalamus and cortex region (Cruikshank et al., 2002) was sliced in icy-cold oxygenated ACSF, using a microtome (Leica VT1200) and transferred into oxygenated ACSF warmed at physiological temperature (35–37°C) for an hour. After recovery, the acute brain slice was transferred to a perfusion chamber cycled with oxygenated ACSF at room temperature for imaging. The refractive index of the ACSF is 1.33. The objective lens was immersed into the perfusion chamber during the imaging.

References

1. L. Tian, S. A. Hires, T. Mao, D. Huber, M. E. Chiappe, S. H. Chalasani, L. Petreanu, J. Akerboom, S. A. McKinney, E. R. Schreiter, C. I. Bargmann, V. Jayaraman, K. Svoboda, L. L. Looger, Imaging neural activity in worms, flies and mice with improved GCaMP calcium indicators. *Nat. Methods*. **6**, 875–881 (2009).

2. T.-W. Chen, T. J. Wardill, Y. Sun, S. R. Pulver, S. L. Renninger, A. Baohan, E. R. Schreiter, R. A. Kerr, M. B. Orger, V. Jayaraman, L. L. Looger, K. Svoboda, D. S. Kim, Ultrasensitive fluorescent proteins for imaging neuronal activity. *Nature*. **499**, 295–300 (2013).

3. J.-D. Pédelacq, S. Cabantous, T. Tran, T. C. Terwilliger, G. S. Waldo, Engineering and characterization of a superfolder green fluorescent protein. *Nat. Biotechnol.* **24**, 79–88 (2006).

4. N. C. Shaner, R. E. Campbell, P. A. Steinbach, B. N. G. Giepmans, A. E. Palmer, R. Y. Tsien, Improved monomeric red, orange and yellow fluorescent proteins derived from Discosoma sp. red fluorescent protein. *Nat. Biotechnol.* **22**, 1567–1572 (2004).

5. R. K. Chhetri, F. Amat, Y. Wan, B. Höckendorf, W. C. Lemon, P. J. Keller, Whole-animal functional and developmental imaging with isotropic spatial resolution. *Nat. Methods*. **12**, 1171–1178 (2015).

6. A. Hernández, V. Nácher, R. Luna, A. Zainos, L. Lemus, M. Alvarez, Y. Vázquez, L. Camarillo, R. Romo, Decoding a Perceptual Decision Process across Cortex. *Neuron*. **66**, 300–314 (2010).

7. Z. V. Guo, N. Li, D. Huber, E. Ophir, D. Gutnisky, J. T. Ting, G. Feng, K. Svoboda, Flow of Cortical Activity Underlying a Tactile Decision in Mice. *Neuron*. **81**, 179–194 (2014).

8. P. S. Tsai, C. Mateo, J. J. Field, C. B. Schaffer, M. E. Anderson, D. Kleinfeld, Ultra-large field-of-view two-photon microscopy. *Opt. Express*. **23**, 13833–13847 (2015).

9. J. Fan, J. Suo, J. Wu, H. Xie, Y. Shen, F. Chen, G. Wang, L. Cao, G. Jin, Q. He, T. Li, G. Luan, L. Kong, Z. Zheng, Q. Dai, Video-rate imaging of biological dynamics at centimetre scale and micrometre resolution. *Nat. Photonics*. **13**, 809–816 (2019).

10. M. Hoffmann, B. Judkewitz, Diffractive oblique plane microscopy. *Optica*. **6**, 1166–1170 (2019).

11. J. N. Stirman, I. T. Smith, M. W. Kudenov, S. L. Smith, Wide field-of-view, multi-region, two-photon imaging of neuronal activity in the mammalian brain. *Nat. Biotechnol.* **34**, 857–862 (2016).

12. M. Clough, I. A. Chen, S.-W. Park, A. M. Ahrens, J. N. Stirman, S. L. Smith, J. L. Chen, Flexible simultaneous mesoscale two-photon imaging of neural activity at high speeds. *Nat. Commun.* **12**, 6638 (2021).

13. W. Shao, K. Kilic, W. Yin, G. Wirak, X. Qin, H. Feng, D. Boas, C. V. Gabel, J. Yi, Wide field-of-view volumetric imaging by a mesoscopic scanning oblique plane microscopy with switchable objective lenses. *Quant. Imaging Med. Surg.* **11**, 98397–98997 (2021).

14. Y. Xue, I. G. Davison, D. A. Boas, L. Tian, Single-shot 3D wide-field fluorescence imaging with a Computational Miniature Mesoscope. *Sci. Adv.* **6**, eabb7508.

15. G. McConnell, J. Trägårdh, R. Amor, J. Dempster, E. Reid, W. B. Amos, A novel optical microscope for imaging large embryos and tissue volumes with sub-cellular resolution throughout. *eLife*. **5**, e18659 (2016).

16. N. J. Sofroniew, D. Flickinger, J. King, K. Svoboda, A large field of view two-photon mesoscope with subcellular resolution for in vivo imaging. *eLife*. **5**, e14472 (2016).

17. A. W. Lohmann, R. G. Dorsch, D. Mendlovic, Z. Zalevsky, C. Ferreira, Space–bandwidth product of optical signals and systems. *JOSA A*. **13**, 470–473 (1996).

18. Z. Zhang, L. Bai, L. Cong, P. Yu, T. Zhang, W. Shi, F. Li, J. Du, K. Wang, Imaging volumetric dynamics at high speed in mouse and zebrafish brain with confocal light field microscopy. *Nat. Biotechnol.* **39**, 74–83 (2021).

19. V. Voleti, K. B. Patel, W. Li, C. P. Campos, S. Bharadwaj, H. Yu, C. Ford, M. J. Casper, R. W. Yan, W. Liang, C. Wen, K. D. Kimura, K. L. Targoff, E. M. C. Hillman, Real-time volumetric microscopy of in vivo dynamics and large-scale samples with SCAPE 2.0. *Nat. Methods*. **16**, 1054–1062 (2019).

20. T. Nöbauer, O. Skocek, A. J. Pernía-Andrade, L. Weilguny, F. M. Traub, M. I. Molodtsov, A. Vaziri, Video rate volumetric Ca2+ imaging across cortex using seeded iterative demixing (SID) microscopy. *Nat. Methods*. **14**, 811–818 (2017).

21. M. Levoy, R. Ng, A. Adams, M. Footer, M. Horowitz, Light field microscopy. *ACM Trans. Graph.* **25**, 924–934 (2006).

22. R. Prevedel, Y.-G. Yoon, M. Hoffmann, N. Pak, G. Wetzstein, S. Kato, T. Schrödel, R. Raskar, M. Zimmer, E. S. Boyden, A. Vaziri, Simultaneous whole-animal 3D imaging of neuronal activity using light-field microscopy. *Nat. Methods*. **11**, 727–730 (2014).

23. K. Wang, D. E. Milkie, A. Saxena, P. Engerer, T. Misgeld, M. E. Bronner, J. Mumm, E. Betzig, Rapid adaptive optical recovery of optimal resolution over large volumes. *Nat. Methods*. **11**, 625–628 (2014).

24. P. J. Keller, A. D. Schmidt, J. Wittbrodt, E. H. K. Stelzer, Reconstruction of Zebrafish Early Embryonic Development by Scanned Light Sheet Microscopy. *Science* (2008), doi:10.1126/science.1162493.

25. M. B. Ahrens, M. B. Orger, D. N. Robson, J. M. Li, P. J. Keller, Whole-brain functional imaging at cellular resolution using light-sheet microscopy. *Nat. Methods*. **10**, 413–420 (2013).

26. J. Huisken, J. Swoger, F. D. Bene, J. Wittbrodt, E. H. K. Stelzer, Optical Sectioning Deep Inside Live Embryos by Selective Plane Illumination Microscopy. *Science*. **305**, 1007–1009 (2004).

27. A. Kumar, Y. Wu, R. Christensen, P. Chandris, W. Gandler, E. McCreedy, A. Bokinsky, D. A. Colón-Ramos, Z. Bao, M. McAuliffe, G. Rondeau, H. Shroff, Dual-view plane illumination microscopy for rapid and spatially isotropic imaging. *Nat. Protoc.* **9**, 2555–2573 (2014).

28. B.-C. Chen, W. R. Legant, K. Wang, L. Shao, D. E. Milkie, M. W. Davidson, C. Janetopoulos, X. S. Wu, J. A. Hammer, Z. Liu, B. P. English, Y. Mimori-Kiyosue, D. P. Romero, A. T. Ritter, J. Lippincott-Schwartz, L. Fritz-Laylin, R. D. Mullins, D. M. Mitchell, J. N. Bembenek, A.-C. Reymann, R. Böhme, S. W. Grill, J. T. Wang, G. Seydoux, U. S. Tulu, D. P. Kiehart, E. Betzig, Lattice light-sheet microscopy: Imaging molecules to embryos at high spatiotemporal resolution. *Science*. **346**, 1257998 (2014).

29. T.-L. Liu, S. Upadhyayula, D. E. Milkie, V. Singh, K. Wang, I. A. Swinburne, K. R. Mosaliganti, Z. M. Collins, T. W. Hiscock, J. Shea, A. Q. Kohrman, T. N. Medwig, D. Dambournet, R. Forster, B. Cunniff, Y. Ruan, H. Yashiro, S. Scholpp, E. M. Meyerowitz, D. Hockemeyer, D. G. Drubin, B. L. Martin, D. Q. Matus, M. Koyama, S. G. Megason, T. Kirchhausen, E. Betzig, Observing the cell in its native state: Imaging subcellular dynamics in multicellular organisms. *Science*. **360**, eaaq1392 (2018).

30. B. Migliori, M. S. Datta, C. Dupre, M. C. Apak, S. Asano, R. Gao, E. S. Boyden, O. Hermanson, R. Yuste, R. Tomer, Light sheet theta microscopy for rapid high-resolution imaging of large biological samples. *BMC Biol.* **16**, 57 (2018).

31. A. K. Glaser, N. P. Reder, Y. Chen, C. Yin, L. Wei, S. Kang, L. A. Barner, W. Xie, E. F. McCarty, C. Mao, A. R. Halpern, C. R. Stoltzfus, J. S. Daniels, M. Y. Gerner, P. R. Nicovich, J. C. Vaughan, L. D. True, J. T. C. Liu, Multi-immersion open-top light-sheet microscope for high-throughput imaging of cleared tissues. *Nat. Commun.* **10**, 2781 (2019).

32. M. B. Bouchard, V. Voleti, C. S. Mendes, C. Lacefield, W. B. Grueber, R. S. Mann, R. M. Bruno, E. M. C. Hillman, Swept confocally-aligned planar excitation (SCAPE) microscopy for high-speed volumetric imaging of behaving organisms. *Nat. Photonics*. **9**, 113–119 (2015).

33. M. Kumar, S. Kishore, J. Nasenbeny, D. L. McLean, Y. Kozorovitskiy, Integrated one- and two-photon scanned oblique plane illumination (SOPi) microscopy for rapid volumetric imaging. *Opt. Express*. **26**, 13027–13041 (2018).

34. C. Dunsby, Optically sectioned imaging by oblique plane microscopy. *Opt. Express*. **16**, 20306–20316 (2008).

35. H. Sparks, L. Dent, C. Bakal, A. Behrens, G. Salbreux, C. Dunsby, C. Dunsby, Dual-view oblique plane microscopy (dOPM). *Biomed. Opt. Express*. **11**, 7204–7220 (2020).

36. J. Kim, M. Wojcik, Y. Wang, S. Moon, E. A. Zin, N. Marnani, Z. L. Newman, J. G. Flannery, K. Xu, X. Zhang, Oblique-plane single-molecule localization microscopy for tissues and small intact animals. *Nat. Methods*. **16**, 853–857 (2019).

37. B. Yang, X. Chen, Y. Wang, S. Feng, V. Pessino, N. Stuurman, N. H. Cho, K. W. Cheng, S. J. Lord, L. Xu, D. Xie, R. D. Mullins, M. D. Leonetti, B. Huang, Epi-illumination SPIM for volumetric imaging with high spatial-temporal resolution. *Nat. Methods*. **16**, 501–504 (2019).

38. E. Sapoznik, B.-J. Chang, J. Huh, R. J. Ju, E. V. Azarova, T. Pohlkamp, E. S. Welf, D. Broadbent, A. F. Carisey, S. J. Stehbens, K.-M. Lee, A. Marín, A. B. Hanker, J. C. Schmidt, C. L. Arteaga, B. Yang, Y. Kobayashi, P. R. Tata, R. Kruithoff, K. Doubrovinski, D. P. Shepherd, A. Millett-Sikking, A. G. York, K. M. Dean, R. P. Fiolka, A versatile oblique plane microscope for large-scale and high-resolution imaging of subcellular dynamics. *eLife*. **9**, e57681 (2020).

39. C. B. Kimmel, W. W. Ballard, S. R. Kimmel, B. Ullmann, T. F. Schilling, Stages of embryonic development of the zebrafish. *Dev. Dyn. Off. Publ. Am. Assoc. Anat*. **203**, 253–310 (1995).

40. R. Kelsh, M. Brand, Y. J. Jiang, C. Heisenberg, S. Lin, P. Haffter, J. Odenthal, M. Mullins, F. V. van Eeden, M. Furutani-Seiki, M. Granato, M. Hammerschmidt, D. Kane, R. M. Warga, D. Beuchle, L. Vogelsang, C. Nüsslein-Volhard, Zebrafish pigmentation mutations and the processes of neural crest development. *Development* (1996).

41. O. Randlett, C. L. Wee, E. A. Naumann, O. Nnaemeka, D. Schoppik, J. E. Fitzgerald, R. Portugues, A. M. B. Lacoste, C. Riegler, F. Engert, A. F. Schier, Whole-brain activity mapping onto a zebrafish brain atlas. *Nat. Methods*. **12**, 1039–1046 (2015).

42. M. Kunst, E. Laurell, N. Mokayes, A. Kramer, F. Kubo, A. M. Fernandes, D. Förster, M. Dal Maschio, H. Baier, A Cellular-Resolution Atlas of the Larval Zebrafish Brain. *Neuron*. **103**, 21-38.e5 (2019).

43. K. Baker, K. S. Warren, G. Yellen, M. C. Fishman, Defective "pacemaker" current (Ih) in a zebrafish mutant with a slow heart rate. *Proc. Natl. Acad. Sci*. **94**, 4554–4559 (1997).

44. W. Shao, J. Yi, *bioRxiv*, in press, doi:10.1101/2021.08.05.455286.

45. L. Zhang, A. Capilla, W. Song, G. Mostoslavsky, J. Yi, Oblique scanning laser microscopy for simultaneously volumetric structural and molecular imaging using only one raster scan. *Sci. Rep*. **7**, 1–11 (2017).

Acknowledgments

Author contributions: J.Y. and W.J.S. conceived the idea. W.J.S and J.Y. built the imaging system and performed the *in vivo* imaging experiment. J.S.M and K.E. prepared the zebrafish samples. P.O.K and M.Z.C prepared the acute brain slice samples. W.J.S and J.Y wrote the manuscript. J.S.M, K.E, P.O.K, and M.Z.C revised the manuscript. J.Y. supervised the entire project.

Competing interests: All other authors declare they have no competing interests.

Data and materials availability: All data are available in the main text or supplementary materials.

Supplementary Materials for

Mesoscopic oblique plane microscopy (Meso-OPM) - enabling large-scale 4D isotropic cellular resolution imaging with a diffractive light sheet

Wenjun Shao, Minzi Chang, Kevin Emmerich, Patrick O Kanold, Jeff S Mumm, Ji Yi

*Corresponding author. Email: jiyi@jhu.edu

The characterization of the magnification, field of view (FOV), and resolution.

The magnification

As the optical system of our experimental setup was designed in accordance with the 4f system, the focal length of the lenses can be used to calculate the lateral magnification which is ~4×. Because the excitation light sheet was not perpendicular to the optical axis, the axial magnification was not able to be calculated in the same way as the lateral magnification but could be calculated according to our previous publication(*44*). The calculated axial magnification of ~ 3.2× was slightly smaller than the lateral. The real magnification in the lateral dimension can be calibrated by imaging rule, and that of the axial can be calibrated by imaging the displacement of the image after moving the sample in the depth direction(*13*). The calibrated results, which were ~4× and ~ 3.2× for lateral and axial direction, respectively, matched well with the calculated results.

The FOV and resolution

After the calibration of magnifications, red and green fluorescent beads with 1 μm diameter dispersed separately in agarose were imaged to evaluate both the FOV and the resolution. The moving aluminum foil was synchronized to block the -1_{st} and 0_{th} excitation during the imaging process (See *Methods* in Main text). 3350 images (2048 (X) × 230 (Z) pixels) were acquired for each kind of fluorescent bead sample. As the illumination light sheet is oblique, the acquired images were oblique cross-sectional images. The real geometry of the acquired volume data was recovered by an affine transformation (See *Methods* in Main text). The imaging results for green and red fluorescent beads under excitation wavelengths of 488 nm and 561 nm are shown in Fig. S1 and S2, respectively. By converting the pixel dimension to the physical size with the calibrated magnifications, the FOV is calculated to be ~3.3 mm (X) × 5.4 mm (Y) × 0. 33 mm (Z). The FOV in the X direction is limited to 3.3 mm (2048×6.5/4) by the sensor size of the camera in our current setup, which is 2048 × 2448 pixels with pixel size of 6.5 μm. As the Y direction is the scanning direction, the FOV doesn't have such limitation as has in the X direction. Projections along the three axes of the volume datasets acquired for the green and red beads are shown in Fig. S1a-c) and Fig. S2 a-c, respectively. The brightness of the image is fairly uniform across the whole FOV expect slight vignetting at the edge of the FOV. Zoom-in views of the XY, XZ, and the YZ projections are provided in Fig. S1d-f) and Fig. S2 d-f). The elongation of the beads along the axial direction is not significant so that the lateral profile of the beads tends to be very similar to that of the axial profile. This is a good indication that the axial resolution is very close to that of the lateral. Besides, the quality of the beads image is well maintained throughout the whole depth of ~330 μm except for minor deterioration due to the broadening of the excitation beam. To further examine the profile of individual beads, three representative beads in different depths are extracted. The projections of each bead are provided in Fig. S1h-j) and Fig. S2h-j) for green and red beads, respectively. The constant image quality of the beads in different depths further suggests that the resolution is well maintained in the accessible depth range. The comparison of the lateral and axial profiles between each bead further confirms that the axial resolution is significantly improved and comparable to that of the lateral. To quantify the resolution, we calculated the full width at half maximum (FWHM) of the line sections through maximum intensity projections of each bead. As for the 488 nm excitation, the average FWHM values across the FOV were 2.7 ± 1.1 (x), 3 ± 1.4 μm (y), 6 ± 1.8 μm (y) (n = 50); as for that of 561 nm excitation, the average FWHM values were 2.9 ± 1 (x), 3.5 ± 1.5 μm (y), 6 ± 1.9 μm (y) (n = 50). Short excitation wavelength has better lateral resolution, which is as excepted. But short excitation wavelength doesn't lead to better axial wavelength. This is probably because the angle of the diffractive light sheet under short excitation wavelength is smaller than that of the longer

wavelength, which in turn cancels the axial resolution improvement under short wavelength. The measured axial resolution is

The axial resolution of an objective lens with NA of 0.3 is limited within ~11 μm under 488nm laser excitation. Therefore, the proposed method breaks this limitation and offers ~2-fold improvement in axial resolution.
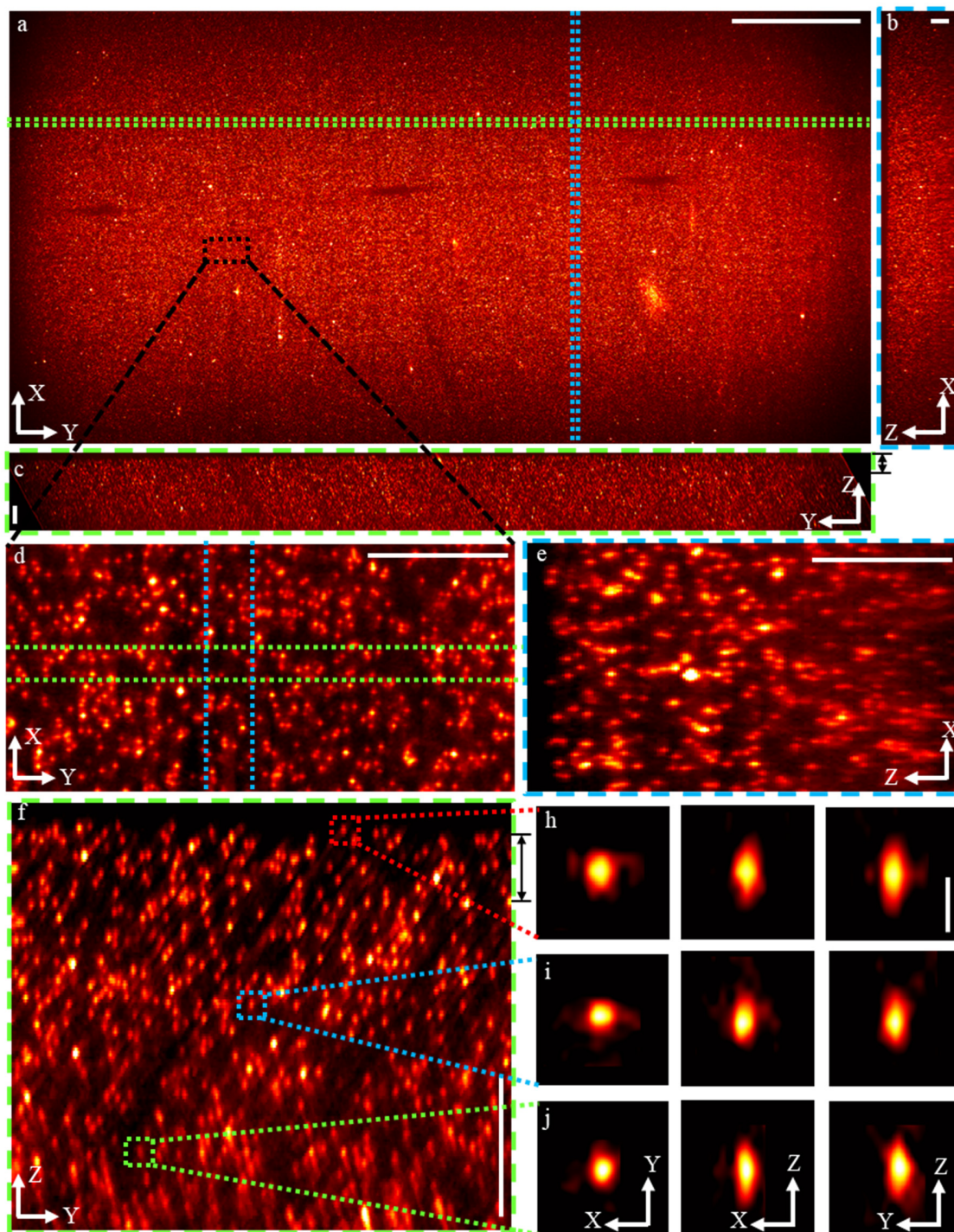

Fig. S1. Resolution and FOV characterization under the blue laser (488 nm) excitation. a) *En face* view generated by the MIP of the area between the black arrow in panel c). b) XZ cross-section generated by MIP of the area between the blue dash lines in panel a). c) YZ cross-section generated by MIP of the area between the green dash lines in panel a). d-f) Three zoom-in projections of the volume area that indicated by the black dashed rectangle in panel a). d) is the *en face* view generated by MIP of the depth layer indicated by the black arrows in panel f). e) and f) are the YZ and XZ cross-sections that are generated by MIP of the area indicated

by the green dash lines and blue dash lines in panel d). The scale bar is 1000 μm for panel a), and the scale bar for the rest panels is 100 μm.
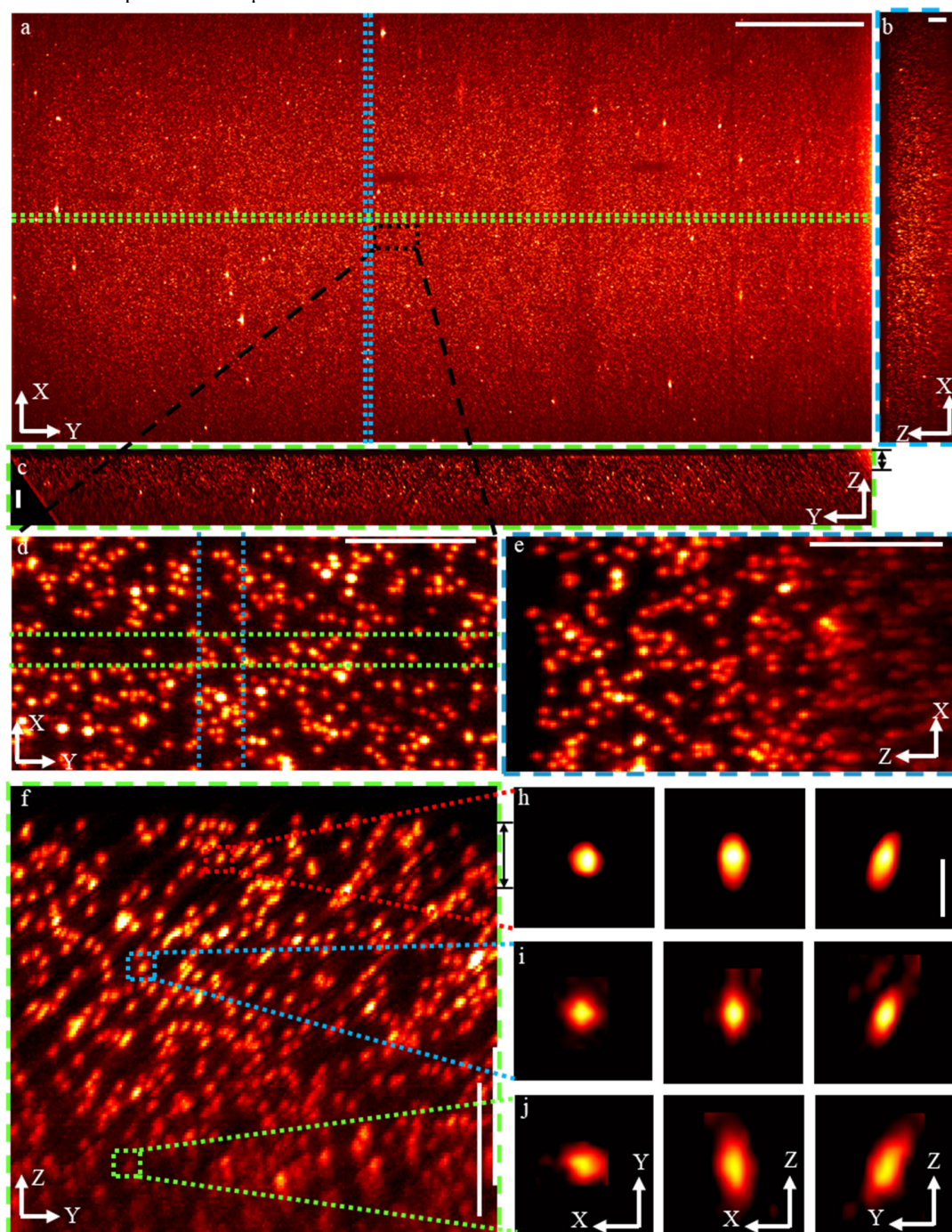

Fig. S2. Resolution and FOV characterization under the blue green (561 nm) excitation. a) *En face* view generated by the MIP of the area between the black arrow in panel c). b) XZ cross-section generated by MIP of the area between the blue dash lines in panel a). c) YZ cross-section generated by MIP of the area between the green dash lines in panel a). d-f) Three zoom-in projections of the volume area that indicated by the black dashed rectangle in panel a). d) is the *en face* view generated by MIP of the depth layer indicated by the black arrows in panel f). e) and f) are the YZ and XZ cross-sections that are generated by MIP of the area indicated by the green dash lines and blue dash lines in panel d). The scale bar is 1000 μm for panel a), and the scale bar for the rest panels is 100 μm.
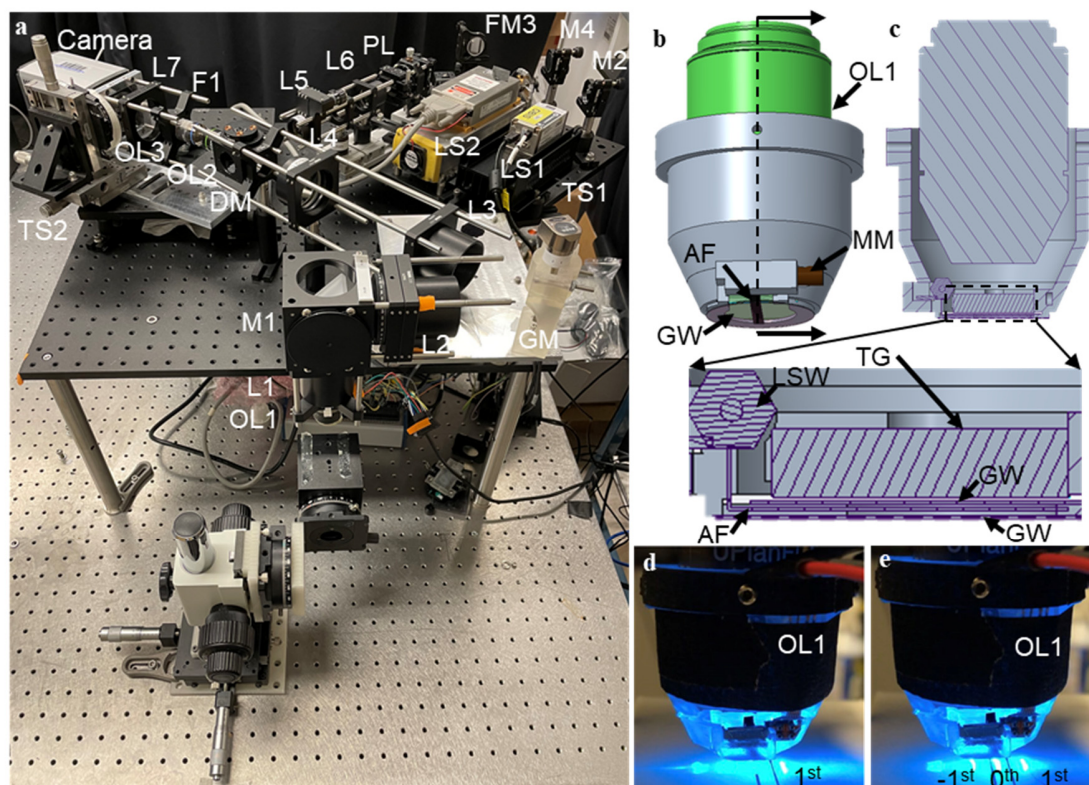
The experiment setup

Fig. S3. The real experiment setup and the 3D model of the primary objective lens. a) The actual photograph of experiment setup; (L: lens; M: mirror; F: filter; PL: Powell lens; LS: light source; DM: dichroic mirror; GM: galvanometer mirror; TS: translation stage;) b) The 3D model of the assembly of the primary objective lens with the transmission grating (TG), aluminum foil (AF), micro-motor (MM), and glass window (GW); c) The cross-section of the assembly in panel (b) showing the alignment of the TG, GW, and AF. The AF is sandwiched between two GW and translated by the MM together with a micro linear stage (only the lead screw (LSW) of the linear stage can be seen); d-e) The real photograph of the assembly. As for panel d, the -1st and 0th orders are blocked by the aluminum foil so that only the 1st order can be used for illumination. As for panel e, the three diffraction orders (-1st, 0th, and the 1st) are not blocked by the aluminum foil.

The actual photograph of the experimental setup is shown in Fig. S3a). Fig. S3b) is the 3D model of the assembly of the primary objective lens (OL1), TG, AF, GW, and MM. To illustrate the working principle of how the diffraction order of -1st and 0th are blocked, the internal structure of the assembly is provided in Fig. S3c). As shown in Fig. S3d), by moving the AF to a proper position, the -1st and 0th orders are blocked while the 1st is still can be used to illuminate the sample. On the contrary, without the engagement of the AF, all the three-diffraction orders can be observed. A video (supplement video 5) is also provided to demonstrate that the AF can be synchronized to block -1st and 0th orders of the moving light sheet.

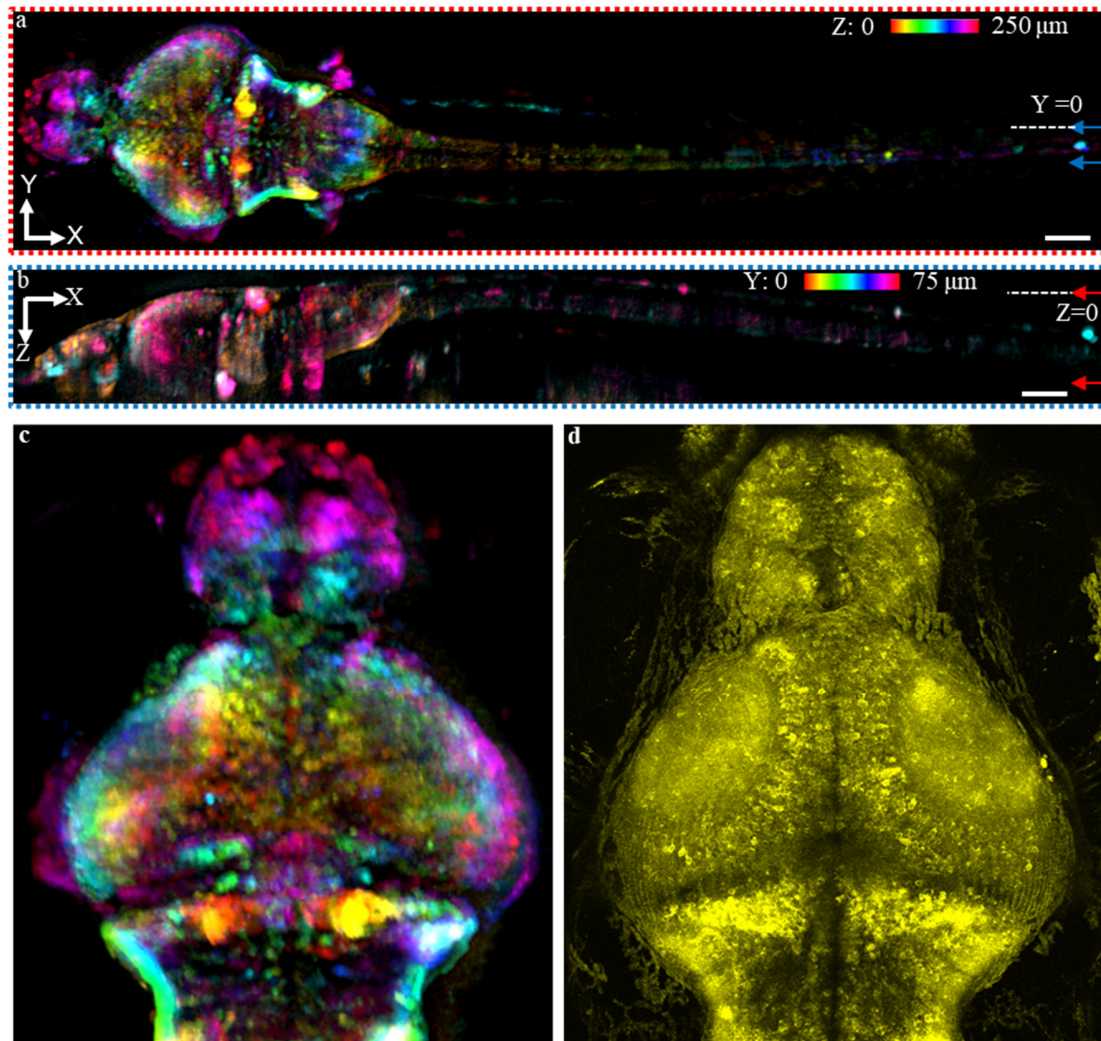**A comparison of the image acquired with Meso-OPM and confocal microscope.**

Fig. S4. Image comparison between Meso-OPM (a-c) and confocal microscope (d). (a) Color-coded MIP in XY plane over 250 μm along the Z dimension. The reference positions of the MIP are marked by arrows in panel b. (**b**) Color-coded MIP in XZ plane over 75 μm in the Y dimension. The reference positions of the MIP are marked by arrows in panel a. c) The zoomed *en face* z-projection imaged by Meso-OPM. e) The *en face* z-projections of a different larval fish imaged by confocal microscope.

To compare the image results with that of the confocal microscope, a zebrafish larva (4dpf, jGCaMP7s) was firstly imaged by Meso-OPM at 100 Hz per plane and scanned 300 planes at ~1.6 μm spacing. The results are shown in Fig. S4a-c. Figure S4d is *en face* z-projections of fish data acquired by a commercial confocal microscope (20X, NA/0.95). As the numerical aperture of the confocal microscope is much higher than that of the Meso-OPM, it offers a better lateral resolution. Individual neurons in the confocal image are much sharper than that of Meso-OPM, which is as expected. Nevertheless, Meso-OPM can still resolve dividual neurons, and similar anatomical organization of neurons can be observed in both images.

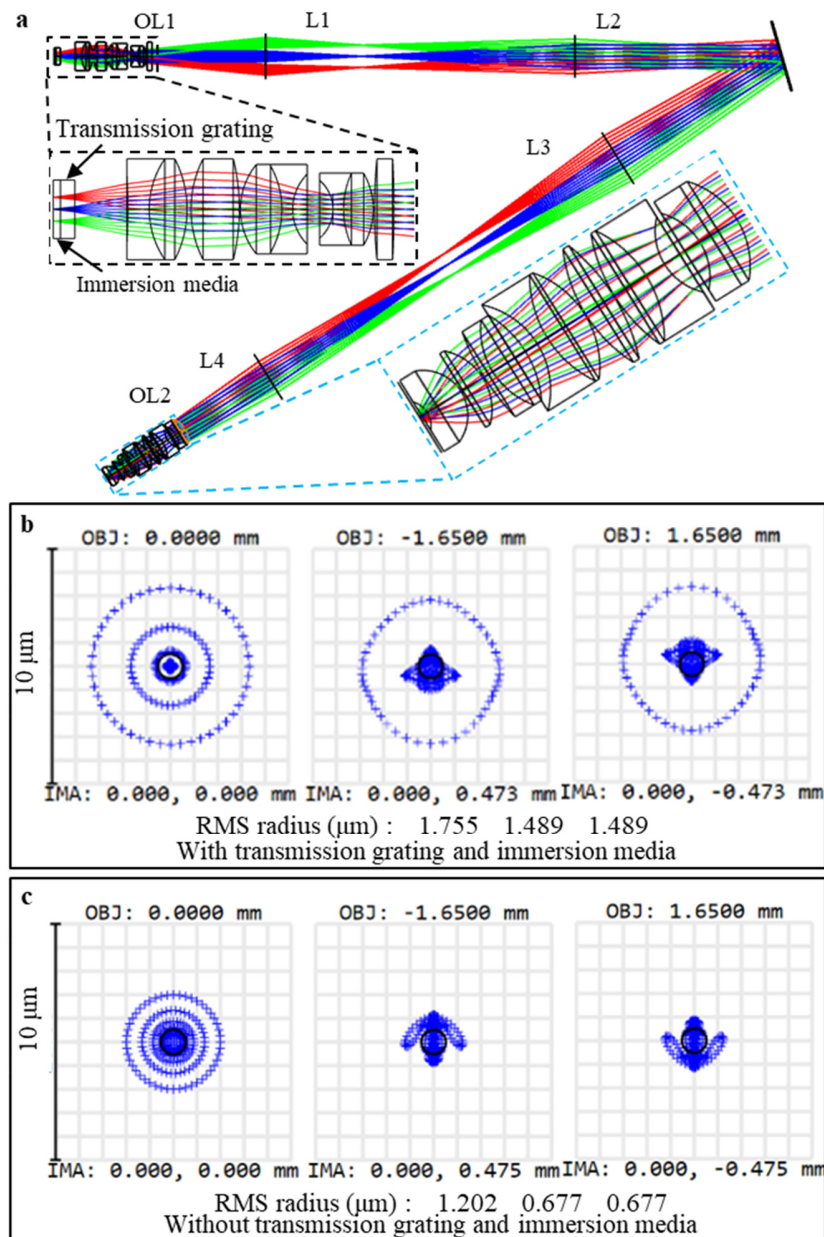## The optical aberration associated with the transmission grating and immersion media

Fig. S5. The evaluation of the optical aberration caused by the transmission grating and the immersion media. a) The layout of the ray-tracing simulation. OL: objective lens; L: lens. b) The spot diagram with transmission grating and immersion media. c) The spot diagram without transmission grating and immersion media. RMS: root-mean-square. RMS is the root-mean-square value of the radius of all the rays.

As the transmission grating has a thickness of ~ 2 mm and is placed underneath the objective lens, it may add additional optical aberration. Optical aberration may also increase as a result of using an air objective lens with immersion media. To evaluate the optical aberration associated with the transmission grating and the immersion media, a ray-tracing simulation shown in Fig. S5a) was designed in Zemax according to the real experimental setup described in the main text. Only the light from the 0th diffraction order of the transmission grating is utilized in the simulation. The thickness of immersion media is 1mm and has a refraction index that is close to that of water. The lens data for the two objective lenses are edited according to the public patents from Olympus. The achromatic lenses used as relay

lenses (L1-L4) in the actual setup are replaced with the idea lens so that the comparison can focus more on the optical aberration transmission that is caused by the grating and immersion media. As only a portion of the light from the OL2 can be collected by the remote focusing system, a reduced numerical aperture of ~0.18 is used in the simulation. The wavelength in the simulation is 510 nm representing the center wavelength of emission spectrum in the green fluorescent protein, and the field point is ± 1.65 mm covering the full FOV in the X-direction. Although the aberration is smaller without the use of transmission grating and the immersion media (Fig. S5b) and c)), the RMS in Fig. S5b) still suggests that the resolution can be maintained within ~1.5 μm when transmission grating and immersion media are used.

The separation of light in different diffraction orders.
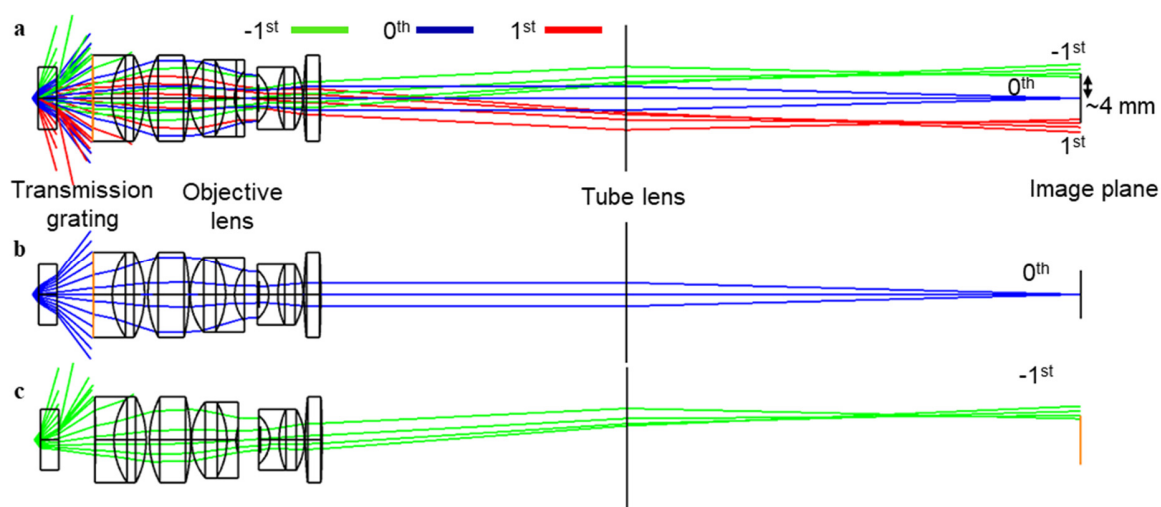

Fig. S6. Ray tracing simulation of imaging with transmission grating. a) Ray tracing simulation showing the images of three different diffraction orders are separated in the image plane. b) Ray-tracing simulations only showing the 0th order. c) Ray-tracing simulations only showing the -1st order.

A ray tracing simulation shown in Fig. S6 is used to explain the separation of three diffraction orders (-1st 0th, and the 1st) generated by the transmission grating. The objective lens was designed according to the lens data of a public patent (10X objective lens) from Olympus. As the overall magnification is ~4X, a paraxial lens with focal length of 72 mm is used to represent all the subsequent optics. As can be seen from Fig. S6a-c, the images of -1st and the 1st are defocused and have a distance of ~4 mm from the focused image of the 0th order. The 4 mm in the image space is equal to ~1 mm in the object space. Because the Rayleigh range of the light sheet is less than 1 mm along the Y direction (The diffraction direction is along the Y direction.), light comes from -1st and the 1st will not affect the image of the 0th order. The beads image in Fig. S1 and S2 also confirm that there are no artifacts caused by light from -1st and the 1st. Please note that the light from the non-zero orders wasn't observed (or was very weak) even when utilizing the whole FOV of the camera which has a sensor size of ~13 mm × 16 mm. The reason might be due to the low diffraction efficiency when the incident angle is large.

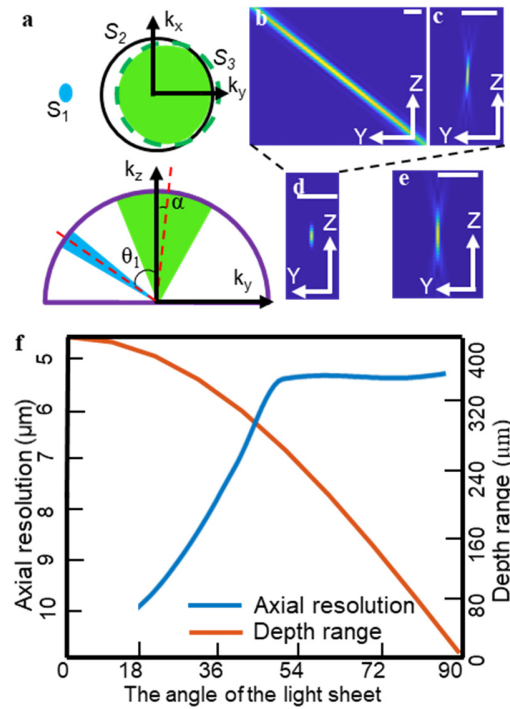## The numerical simulation for axial resolution

Fig. S7. The calculation of the theoretical resolution and the depth detection range of the proposed method. a) The 3D frequency support of the illumination and detection in 3D Fourier domain. b) and c) The Y-Z cross-sections of the illumination and detection PSFs. d) The Y-Z cross-sections of the combined PSF. e) The Y-Z cross-sections of the detection PSF under the full detection NA of 0.3.

To evaluate the diffraction-limited resolution for the proposed method, a Fourier mode according to our previous publication(*44*) is established in Fig. S7a). The coordinate is reciprocal with the Cartesian coordinate (X, Y, Z) that described in the main text (Main text: Fig. 1 and Fig. 6), and can be expressed with a wave vector k,

$$\vec{k} = \frac{2\pi}{\lambda} \hat{k}(k_x, k_y, k_z)$$

(S1)

where $\hat{k}$ is the directional vector with unit magnitude, λ is the wavelength, k_x, k_y, and k_z are the coordinates of the Fourier model, λ is the wavelength of the light source. The blue circle S_1 and the white circle S_2 represent the spatial frequency range for the illumination and the primary objective lens OL1 (See Fig. 6 in the main text), respectively. The dash green circle S_3 shows the equivalent frequency range of the OL$_3$ (See Fig. 6 in the main text) that is mapped on the back aperture of OL1. The overall spatial frequency range for the detection is illustrated by the intersection area of S_2 and S_3.

The effective numerical aperture (NA) of the illumination on the primary objective lens can be calculated by $NA_I = R_I/f_{obj}$ in which R_I (~0.8 mm) is the radius of the beam that is projected on the back aperture of OL1, and f_{obj} (18 mm) is the focal length of the primary objective lens. The angle θ_I (51º for 488 nm laser, and 60º for 561 nm laser) of the illumination can be calculated by the grating equation given in the main text (Main text: Eq(1)). So the special frequency range for the illumination S_I is identified as:

$$(k_x)^2 + (k_y)^2 + (k_z)^2 = (2\pi/\lambda)^2,$$

$$\{(kx, ky) \mid \sqrt{k_x^2 + (k_y - \sin\theta_1 \times 2\pi/\lambda)^2 + (k_z - \cos\theta_1 \times 2\pi/\lambda)^2} \leq (2\pi/\lambda)NA_I\} \quad (S2)$$

As the back aperture of the OL2 (See Fig. 6 in the main text) is proximately matched with that of OL1, the equivalent collection NA of OL3 mapped on OL1 can be given as :

$$NA_D = NA_{OL1}NA_{obj3} / NA_{obj2}, \quad (S3)$$

where $NA_{OL1}(0.3)$, $NA_{OL2}(0.75)$, and $NA_{OL3}(0.75)$ is the NA of the OL1, OL1, and OL3, respectively. The angle α between S2 and S3 is due to the non-axial alignment OL2 and OL3, which can be estimated as follows:

$$\alpha = \beta \times NA_{OL1} / NA_{obj2}, \quad (S4)$$

where β (11º for 488 nm excitation and 8º for 561 nm excitation) is the angle between the optical axis of the OL2 and OL3. After specified NA_D and α, S2 can be defined as:

$$(k_x)^2 + (k_y)^2 + (k_z)^2 = (2\pi/\lambda)^2,$$

$$\{(kx, ky) \mid \sqrt{k_x^2 + (k_y + \sin\alpha \times 2\pi/\lambda)^2 + (k_z + \cos\alpha \times 2\pi/\lambda)^2} \leq (2\pi/\lambda)NA_D\} \quad (S5)$$

Given the NA of OL1 (NA = 0.3), S3 can be written as:

$$(k_x)^2 + (k_y)^2 + (k_z)^2 = (2\pi/\lambda)^2,$$

$$\{(kx, ky) \mid \sqrt{k_x^2 + (k_y)^2 + (k_z - 2\pi/\lambda)^2} \leq (2\pi/\lambda)NA_{OL1}\} \quad (S6)$$

The overall spatial frequency range for the detection can be obtained by combing Eq (S5) and (S6). After the description of the 3D frequency support, the illumination and the detection point spread function (PSF) can be obtained by performing 3D Fourier transformation (Fig. S7, b-c). The combined system PSF is a production of the illumination and the detection PSF. As for 488 nm laser excitation, the calculated theoretical resolutions are ~1 μm (X) × 1.5 μm (Y) × 5 μm (Z). The YZ cross-section of the system PSF is shown in Fig. S7d). The detection PSF from the full NA (0.3) of the OL1 has a FWHM of ~11 μm in the Z dimension (Fig. S7e), which can be calculated by the same method described above. According to the comparison in Fig. S7d-e, the proposed method can offer 2 times better axial resolution than the diffraction-limited axial resolution of OL1. This also match well with the results shown in Fig. S1 and S2.

To guide the choice of the line density of the transmission grating, we simulated axial resolution under different illumination angles of θ_I. To simplify the calculation, we only change the θ_I while keeping the detection NA_D and α same as the above calculation. The change of axial resolution as a result of the different illumination angles is shown in Fig. S6.f). There is a sharp increase in the axial resolution from 20º to 60º while the increment slows down when the angle is large than 60º. The axial resolution is not provided for the angle below 20º because the light collection issue of the remote focusing system will lead to axial resolution larger than 34 μm(*10, 13*).

The angle of the illumination also affects the axial detection range (Fig. S6f), which can be calculated by $b \times \cos\theta_I$, in which b is the Rayleigh range. As for the current experiment,

we chose a transmission grating with a line density of 0.83 μm/line to keep a balance between the axial resolution and the axial detection range.
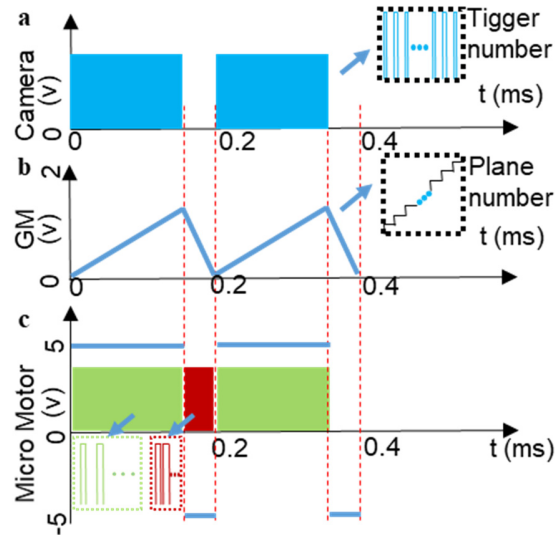
The control signals

Fig. S8. The control signals for the experiment setup. a-c) are the control signals for the camera external trigger, the galvanometer mirror, and the micro-motor, respectively.

The control signals for the experimental setup are shown in Fig. S8. The external triggers (Fig. S8a) for the camera are only generated in the forward scanning (Fig. S8b) of the galvanometer mirror. There will be an image acquired by the camera after each external trigger signal. Each external trigger for the camera is synchronized with an increment in the voltage signal for the galvanometer mirror. A volume data set will be acquired at the end of backward scanning. To block the -1st and 0th diffraction orders, the movement of the micro-motor is synchronized with the light sheet. The blue lines in Fig. S8c represent the rotation direction of the micro-motor while the green pluses are corresponding to each micro-step of the micro-motor.

Movie S1.

3D rendering of live zebrafish larva data obtained in a single FOV

Movie S2.

3D rendering of acute brain slice over a single FOV of 3.3 mm (X) × 5.4 mm (Y) × 0.33 mm (Z).

Movie S3.

4D rendering of whole-body neuronal activity recorded in zebrafish larva with isotropic cellular resolution at volume rate of 2 Hz (The first 7s is 3D rendering, and the rest part is 4D rendering for ~1.5 min but plays at 4.5× speed.)

Movie S4.

4D rendering of whole-body blood flow recorded in zebrafish larva with isotropic cellular resolution at volume rate of 5 Hz (play at 1× speed.)